J Ther Eng, Vol. 11, No. 4, pp. 1093−1118, July, 2025

Journal of Thermal Engineering
Web page info: https://jten.yildiz.edu.tr
DOI: 10.14744/thermal.0000966

Research Article

The impact of electrode design parameters on the thermal behavior of a lithium-ion battery

Ahmed Fouad AL-NEAMA[1,*], **Harvey Morpeth THOMPSON**[2]

[1]*Department of Mechanical Engineering, College of Engineering, University of Mosul, 41002, Iraq*
[2]*Institute of Thermofluids, School of Mechanical Engineering, University of Leeds, LS2 9JT, United Kingdom*

ARTICLE INFO

Article history
Received: 14 May 2024
Revised: 18 August 2024
Accepted: 20 August 2024

Keywords:
18650-type NMC Battery; Discharge Rate; Electrode Thickness; LiB; State of Charge

ABSTRACT

The main objective of this study is to develop an accurate simulation methodology for the temperatures in cylindrical lithium-ion batteries (LiBs), while they are being continuously charged and discharged, that can be used to ensure they remain within safe operating limits. A comprehensive 3D simulation methodology for air-cooled cylindrical LiBs is developed and applied to the specific case of an 18650-type NMC LiB. The battery cell chemistry is modelled using a Pseudo 2D electrochemical model, while the temperature within the battery is represented using a 3D axisymmetric heat transfer model. The electrochemical and thermal behaviours are modelled by coupling the heat source produced from the electrochemical model with the average temperature from the thermal model. This study's key novelty lies in its detailed investigation into how multiple electrode design parameters affect the LiB's thermal characteristics. To verify the model's accuracy, the simulation outcomes are compared with experimental data on discharge voltage and surface temperature of LiBs at different discharge rates, and good agreement is obtained. The model is then used to explore the impacts of the electrode thickness, positive electrode particle size, charge-discharge rate (C-rate) and inlet airflow velocity on battery thermal behaviour. The numerical results revealed that increasing the C-rate, electrode thickness, and positive electrode particle size increases the LiBs' temperature rise rate; however, increasing inlet airflow velocity reduces the temperature rise of the battery cell. At inlet airflow velocity of 0.1 m/s, the maximum temperature roughly increases by 31.7 °C (at 6 C-rate) compared to the 1 C-rate case. At 4 C-rate and inlet airflow velocity of 0.2 m/s, the numerical results predict that increasing the negative electrode thickness from 25 to 70 µm increased the maximum temperature from 31.8 to 48.1 °C, while raising positive electrode particle size from 1 to 7 μm increased the maximum temperature from 32.06 °C to 38.74 °C (at time of 2000 s). The research method and conclusions can provide valuable references for further research on the thermal characteristics of the LiB.

Cite this article as: Al-Neama AF, Thompson HM. The impact of electrode design parameters on the thermal behavior of a lithium-ion battery. J Ther Eng 2025;11(4):1093−1118.

***Corresponding author.**
*E-mail address: ahmedfalneama@uomosul.edu.iq

This paper was recommended for publication in revised form by Editor-in-Chief Ahmet Selim Dalkılıç

Published by Yıldız Technical University Press, İstanbul, Turkey

INTRODUCTION

It is recognized that the widespread use of internal combustion engines has resulted in severe environmental impacts and negative health effects on humans [1]. This has provided the impetus to replace traditional automobiles with electric vehicles (EVs), which can reduce the associated greenhouse gas (GHG) emissions and improve air quality [2]. By 2045, most vehicles in the U.S. are predicted to be hybrid electric vehicles (HEVs) or plug-in hybrid electric vehicles (PHEVs) [3]. Lithium-ion batteries (LiBs) currently dominate the market for EVs in passenger vehicles due to their low self-discharge rate, low cost, greater stability, larger capacity with reduced weight, nontoxicity, and higher power [4]. However, the accumulation of heat that is generated by the LiB during operation can cause overheating of the battery pack and uneven temperature distribution within LiBs, resulting in a reduction in in battery capacity and a reduction in operating life [5]. For example, several studies have shown that high temperatures significantly above 40 °C can reduce battery life significantly and can even result in irreversible temperature rises (thermal runaway) that presents severe safety concerns which can ultimately result in fires and explosions [6]. As a result, battery thermal management system (BTMS) is critical in the realm of modern energy vehicles and energy storage, particularly during fast charging or in hot weather conditions [7].

Thermal management solutions are essential for various practical applications involving batteries. Proper thermal management ensures optimal performance, safety, and longevity of battery systems in diverse fields. EVs, renewable energy storage, aerospace and aviation, grid energy storage, and military and defense are some practical applications and examples of thermal management solutions.

As batteries become more prevalent in a variety of applications, innovative BTM technologies are emerging to meet the challenges associated with heat generation and dissipation. Different cooling techniques have distinct limitations and benefits. Air cooling, liquid cooling, phase change material (PCM) cooling, and heat pipe cooling are four common cooling strategies in BTMS [8]. Air cooling system (with natural or forced convection) has a simple design, low cost, and high commercial maturity. However, air cooling has low specific heat, thermal conductivity, and heat dissipation capacity [9]. Although forced-air cooling is widely used in practical applications and can mitigate temperature rise, it will inevitably result in a huge nonuniform temperature distribution within the LiB cell at high operational temperatures and throughout aggressive driving circles. Nevertheless, air cooling is adequate in some cases, such as parallel HEVs. A liquid cooling technique is more efficient, however due to its cost, complexity, and the possibility of leakage, manufacturers are hesitant to use it [10]. PCM-based cooling is also more efficient because of its higher latent heat [11]. However, adding PCM to a LiB pack could add undesired volume and mass, is flammable, and prone to leakage [12]. PCMs also need to release the heat that they accumulate while cycling continuously, but they are capable of handling extreme temperatures. As a result, PCM cooling is typically integrated with other cooling technologies [13]. Heat pipe cooling method for LiB pack is restricted by weight, gravity and passive control [14]. Air, liquid, and fin cooling systems are now the most preferred technologies for electric drive vehicles (EDVs). Some companies, like Toyota Prius, Nissan, and Honda Insight, continue to use air-cooled HEV battery packs as a TMS [15].

Lithium-nickel-cobalt-aluminum-oxide ($LiN_{1-x-y}Co_xAl_yO_2$, *NCA*) and lithium-nickel-manganese-cobalt-oxide ($LiNi_{1-x-y}Mn_yCo_xO_2$, *NMC*) electrodes have recently been developed as alternatives to conventional lithium-iron-phosphate ($LiFePO_4$, *LFP*) ones because of their faster charge/discharge rate and larger specific capacity [16]. However, *NMC* type batteries have a tendency to overheat, particularly when subjected to high current density discharge, leading the LiB's internal temperature to rapidly increase. Despite several studies having explored the thermal behavior of a single battery cell, it is still a challenge to directly monitor the temperature profile within the battery at various current densities. As a result, accurate battery pack thermal modelling is an important requirement for ensuring battery thermal safety.

Many researches have been carried out in recent years to investigate and optimize the impact of electrode design parameters on LiB performance. At present, the quantitative optimization of thickness variations in electric and thermal performance, particularly for cylindrical batteries, has remained an unresolved challenge. Researchers are eager to determine the optimal thickness of electrodes for a given cooling method to prevent excessive temperature increases, which can significantly impact electrochemical performance [17].

Xiao et al. [18] explored monodispersed and uniform cubic $LiMn_2O_4$ with a side length of 5 μm and spherical $LiMn_2O_4$ with diameters ranging between 2 and 8μm. From the finding, it is revealed that the electrochemical performance of $LiMn_2O_4$ samples with spherical morphology is superior to that of cubic samples. Furthermore, mid-sized spherical $LiMn_2O_4$ (3.5 μm in diameter) exhibits the best electrochemical performance. Wang et al. [19] investigated the cycling stability of $Li_{1.06}Mn_2O_4$ with various particle sizes ranging from nano (100-200 nm) to micrometre (2-4 μm) in an aqueous electrolyte at temperatures of 25 °C and 60 °C. Regardless of particle size, the electrochemical tests demonstrate that $Li_{1.06}Mn_2O_4$ has nearly identical cycling stability and rate capability at 25 °C, however there is a substantial variation at 60 °C: after 50 cycles, $Li_{1.06}Mn_2O_4$ with large particle sizes (2-4 μm) exhibits substantially superior cycling stability, with a capacity retention rate of 93%, whereas the sample with nano particle sizes has lower cycling stability, with a capacity retention rate of 78% between 0 and 0.92 V.

Lu et al. [20] claimed that enlarging the thickness of the $LiNi_{0.8}Co_{0.15}Al_{0.05}O_2(NCA)$ cathode material has the capability of increasing the LIB's energy density. Miranda et al. [21] optimized the performance of seven distinct LiB geometries. These diverse geometries include conventional, interdigitated batteries, as well as unique geometries like horseshoe, spiral, ring, antenna, and gear batteries. It is demonstrated that geometrical features such as the maximum distance for ions to travel to the current collector, the distance between current collectors, and the thickness of the separator and electrodes all have an impact on battery capacity. Drake et al. [22] utilized temperature and heat flux sensors to monitor the heat generation rate in a 26650-sized cylindrical LiB at a larger discharge rate (up to 9.6 C). They also investigated the effect of cooling conditions on heat generation. Dasari and Eisenbraun [23] investigated the impact of electrolyte volume fraction (ε_e) and anode particle size (R_p^-) on the performance of silicon anode-based batteries in conjunction with two distinct cathodes, *NCA* and $LiNi_{1/3}Mn_{1/3}Co_{1/3}O_2(NMC\ 111)$. The results showed that when the active particles were less than 150 nm in size, the performance of silicon anode solid active particles could be increased. Optimized ε_e values in the negative electrode, which were determined to be between 0.40 and 0.55, resulted in minimal Li-ion accumulation. Furthermore, *NMC* outperforms *NCA* in terms of relative capacity when utilized in conjunction with a silicon anode.

The 18650 form factor, characterized by its relatively high energy density, is a promising configuration for battery design. The specific chemistry employed in conjunction with graphite anodes, consisting of *NMC* (Nickel Manganese Cobalt oxide), offers a favorable balance between capacity and overall energy density. The widespread availability of 18650 cells in the market, owing to their standard size, provides a convenient option for manufacturers, as they can easily source the necessary components. Furthermore, *NMC* chemistry is known for its stability and safety compared to some other lithium-ion chemistries [24]. Therefore, a commercial 18650 cylindrical *NMC*-graphite Li-ion battery cell with a nominal capacity of 1.78 Ah has been considered in this study.

There have been few previous studies into the influence of multiple electrode design parameters on the electrochemical and thermal performance of LiBs using an *NMC* 111 cathode. The majority of these were aligned towards studying the effect of a single electrode design parameter (i.e., electrode thickness ($L^{\mp}$) and active material particle size ($R_p^{\mp}$)) on the performance, energy density, and power density of LiBs. The present study addresses this research gap by investigating the impact of anode and cathode electrode thicknesses ($L^{\mp}$) and positive electrode particle size (R_p^+) on the LiB's thermal characteristics. A comprehensive set of results demonstrates the influence of electrode design parameters (i.e., $L^{\mp}$ and R_p^+) on the thermal characteristics of a LiB throughout continuous cycles of charge and discharge processes at different C-rates and exposed to varying external cooling conditions.

The key innovation in the modelling methodology is the coupling of both a pseudo-2D (P2D) electrochemical model and a three-dimensional (3D) thermal model utilizing the COMSOL Multiphysics modelling platform at different C-rates and exposed to varying external cooling conditions. Since weight, space, and cost constraints must be considered in EV applications, the methodology is suitable for air-cooled battery packs in EVs, where decreasing peak temperature and enhancing thermal consistency are vital for the batteries' safe and dependable functioning.

ELECTROCHEMICAL-THERMAL COUPLED BATTERY MODEL

Lithium-Ion Battery's Structure

A LiB, including an electrolyte (EL), is utilized to transform chemical energy into electrical energy, and vice versa. A battery cell's fundamental configuration consists of a negative electrode (NE) and a positive electrode (PE) submerged in a non-aqueous EL with a porous separator in between. The NE and PE, which are composed of porous materials, are known as the anode and cathode, respectively. Current collector plates (CCPs) are used to connect the battery to an external load. A copper current collector (CCC) is utilized in the NE of Li-ion cells, while an aluminum current collector (ACC) is used in the PE [25].

The porous negative electrode with spherical graphite particles (i.e., Li_xC_6) provides electrons to the load (external circuit). The porous positive electrode is typically constructed of metal oxides and contains spherical active material particles such as lithium-nickel-manganese-cobalt-oxide, $LiNi_{1/3}Mn_{1/3}Co_{1/3}O_2$ (*NMC* 111), lithium-cobalt-oxide, $LiCoO_2(LCO)$, lithium-manganese-oxide, $LiMn_2O_4$ (*LMO*), Lithium-iron-phosphate, $LiFePO_4$ (*LFP*) and lithium-nickel-cobalt-aluminium-oxide, $LiNi_{0.8}Co_{0.15}Al_{0.05}O_2$ (*NCA*). The separator is a porous membrane, typically made of plastic or ceramic, allowing only Li-ions (Li^+) to transfer and thus acting as a barrier between the electrodes. It needs to be ionically-conductive and electrically-insulating to keep thermal runaway and short-circuits from happening, while also providing minimal resistance. The EL is usually a non-aqueous liquid- or gel-based solution that the two electrodes are submerged in which acts as a conductor allowing the Li-ion cells to move between the anode and the cathode. Typical ELs may include a mixture of alkyl carbonates (such as ethylene carbonate (EC), dimethyl carbonate (DMC), diethyl carbonate (DEC), and ethyl methyl carbonates (EMC)) and lithium hexafluoro-phosphate ($LiPF_6$) salt [26].

Redox (Reduction - Oxidation) reactions take place in the presence of a load current. At the anode, the confined lithium particles begin to diffuse (or deintercalate) towards the EL-solid interface, dividing lithium into *Li*⁺ and electrons. Because of the potential difference, Li-ions migrate through the solution, whereas electrons transfer via the current collector (CC) because the EL solution functions as an electronic insulator. The reduction reaction occurs at the cathode, when the travelling Li-ions from the anode begin to react (or intercalate) with the electrons coming from the positive CCP. The entire intercalation and deintercalation process is reversible since Li^+ travels in both directions between the electrodes while charging and discharging [27]. This phenomenon might, in theory, continue indefinitely. Unfortunately, the capacity and power capabilities of the LiB decay with the number of usages and charges at high rates due to cell substance deterioration and other irreversible chemical reactions [28]. The electrochemical reactions that occur at the electrode/electrolyte interface in both the negative and positive electrodes during discharge/charge for LiB using $Li_yNi_{1/3}Mn_{1/3}Co_{1/3}O_2$($NMC$ 111) in the positive electrode and Li_xC_6 in the negative electrode as the active materials are given by:

$Anod(\ half\ reaction)$:

$$Li_xC_6 \xrightleftharpoons[\text{charge}]{\text{discharge}} Li_{x-z}C_6 + zLi^+ + ze^-$$

$Cathode\ (half\ reaction)$:

$$Li_{y-z}Ni_{1/3}Mn_{1/3}Co_{1/3}O_2 + zLi^+ + ze^- \xrightleftharpoons[\text{charge}]{\text{discharge}} Li_yNi_{1/3}Mn_{1/3}Co_{1/3}O_2$$

$Cell\ (Full\ reaction)$:

$$Li_xC_6 + Li_{y-z}Ni_{1/3}Mn_{1/3}Co_{1/3}O_2 \xrightleftharpoons[\text{charge}]{\text{discharge}} Li_{x-z}C_6 + Li_yNi_{1/3}Mn_{1/3}Co_{1/3}O_2$$

where x and y are the stoichiometric coefficients or moles of lithium contained in the graphite structure (C_6) and the NMC 111, respectively, while z is the number of moles of Li-ions taking part in the electrochemical reaction.

A Pseudo-2D Electrochemical Model

The coupled mathematical model is comprised of a P2D electrochemical portion and a 3D thermal part, in which the heat generated from the electrochemical part and the temperatures obtained from the thermal part are inputs to each other [27]. Figure 1 gives a schematic representation of a LiB unit cell's internal structure during the charge process, as well as the heat generated by LiB. The cell properties considered in the present work are taken in terms of a graphite electrode (Li_xC_6) mesocarbon microbeads ($MCMB$) for anode, lithium hexafluorophosphate ($LiPF_6$) dissolved in a mixture of 3:7 EC:EMC is commonly used as the liquid electrolyte in LiBs, and $LiNi_{1/3}Mn_{1/3}Co_{1/3}O_2$($NMC$ 111) is used for the cathode, while aluminum and copper are the materials for the current collector.

Assumptions, Governing Equations and Boundary Conditions for A LIB Cell

The electrochemical model relies on the following simplifying assumptions [4,27,29]:

1. The electrodes' active material particles are spherical and homogenous in size.
2. The electrodes' volume change during the discharge process is negligible.
3. During the charge/discharge process, no gas is generated.
4. All side reactions are ignored.
5. Li dendrites and the solid electrolyte interphase (SEI) layer formation are negligible.

The electrochemical kinetics, charge and mass conservation in both the solid and electrolyte phases are used within the P2D electrochemical model. The conservation equations for the solid and electrolytes phases are as follows [27,29]:

Charge Conservation Equations

The charge conservation is explained by the ionic movement of Li^+ in the electrolyte phase and the electron transport in the solid phase, which follow concentrated solution theory and Ohm's law, respectively. The concentrated solution theory is based on the concentration change caused by mass flux and reactions. The charge conservation in the positive and negative electrodes is governed by the following equations:

$$\frac{\partial i_s(x,t)}{\partial x} + \frac{\partial i_e(x,t)}{\partial x} = 0 \tag{1}$$

$$\frac{\partial i_s(x,t)}{\partial x} = -\,a_s j_{loc}(x,t) \tag{2}$$

$$\frac{\partial i_e(x,t)}{\partial x} = a_s j_{loc}(x,t) \tag{3}$$

Based on the radius of the active particles ($R_p^{\mp}$) and the volume fraction of the solid phase ($\varepsilon_s^{\mp}$), the solid/electrolyte interfacial area per unit volume (a_s) can be computed, $a_s = 3\,\varepsilon_s^{\mp}/R_p^{\mp}$. The local charge transfer current density (j_{loc}) is function of both x-direction and time (t). The electrical current density in the solid phase (i_s) and the ionic current density in the electrolyte phase (i_e) can be represented as:

$$i_s = -\,\sigma_s^{eff,\mp}\frac{\partial \phi_s^{\mp}(x,t)}{\partial x} \tag{4}$$

$$i_e = -\,\sigma_e^{eff,i}\frac{\partial \phi_e^{i}(x,t)}{\partial x} + \frac{2R_oT\sigma_e^{eff,i}}{F}\left(1 + \frac{dln\, f_{\pm}}{dln\, C_e(x,t)}\right)(1 - t_c^0)\frac{\partial ln\, C_e^i(x,t)}{\partial x} \tag{5}$$

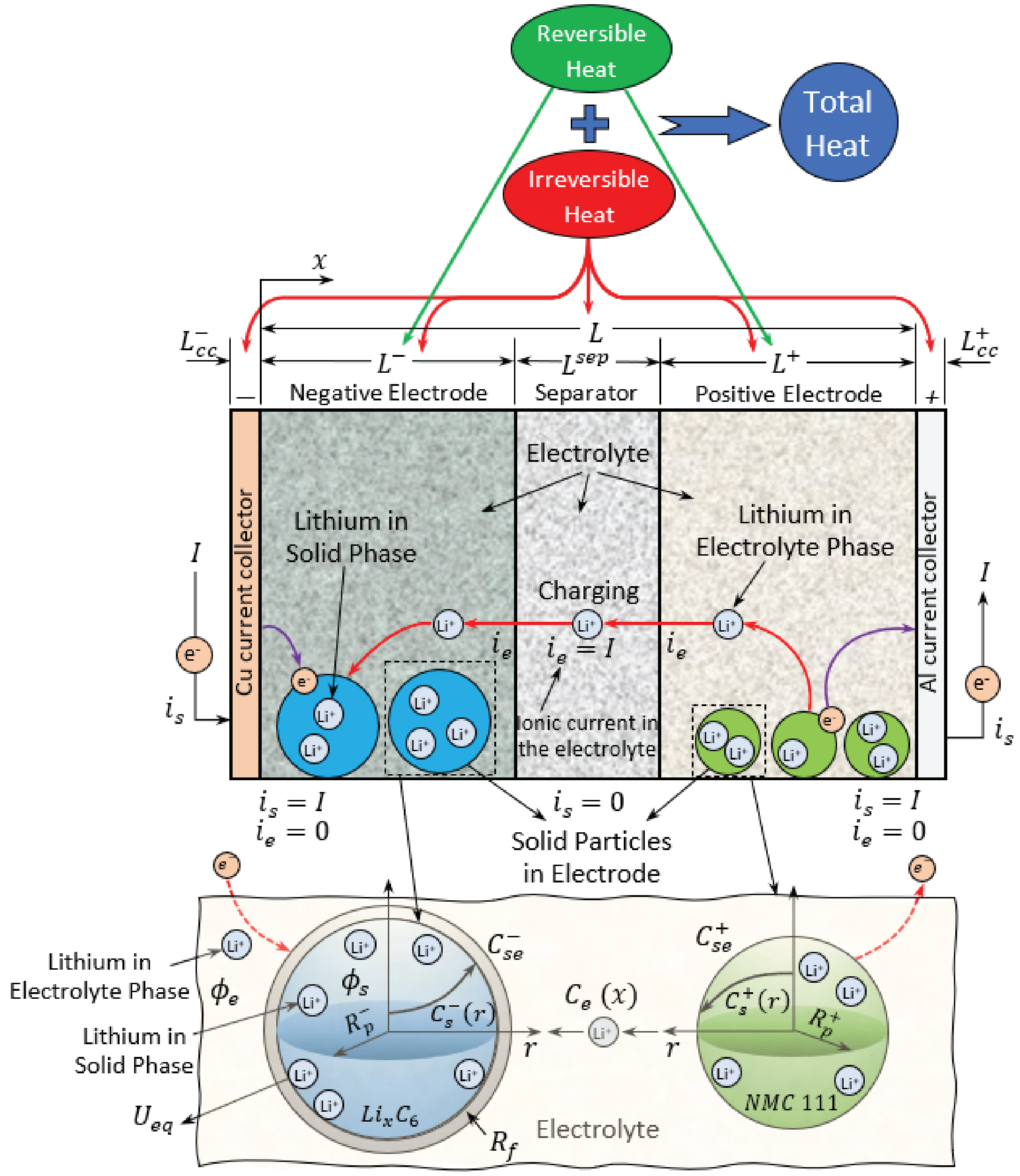

Figure 1. Schematic of the P2D electrochemical model geometry scheme of a lithium-ion cell during charge and heat generating sources in a LiB.

$\phi_s^{\mp}$ and ϕ_e^{i} are the electrical potential in the solid phase and the ionic potential in the electrolyte phase, respectively. The superscript $\mp$ specifies whether the equation is solved for the negative or positive electrode, while the superscript $i \in \{-, sep, +\}$ denotes the negative electrode, separator, and positive electrode, respectively. $C_e^i(x,t)$ denotes the Li-ion concentration in the electrolyte. R_0 is the universal gas constant ($R_o = 8.314$ $J/(mol \cdot K)$), T is the cell temperature in Kelvin, and F is the Faraday's constant ($F = 96{,}487$ $A.s/mol$). t_c^0 is the transference number of the cations with respect to the solvent velocity, and $f_{\pm}$ is the mean molar activity coefficient of the electrolyte, assumed to be constant in the present work.

$\sigma_s^{eff,\mp}$ and $\sigma_e^{eff,i}$ indicate the solid phase material's effective electronic conductivity and the electrolyte's effective ionic conductivity, respectively, which can both be computed by:

$$\sigma_s^{eff,\mp} = \sigma_s^{\mp} \varepsilon_s^{\beta,\mp} \tag{6}$$

$$\sigma_e^{eff,i} = \sigma_e^{i} \varepsilon_e^{\beta,i} \tag{7}$$

where $\sigma_s^{\mp}$ and σ_e^i refer to the bulk electronic conductivity and the ionic conductivity for the binary electrolyte, respectively. ε_s and ε_e represent the volume fraction of solid phase and electrolyte, respectively. To account for the electrode's porosity and tortuosity, $\sigma_s^{eff,\mp}$ and $\sigma_e^{eff,i}$ are corrected with the Bruggeman tortuosity exponent (β), and in this study is assumed to be 1.5 for both the electrodes and separator [16].

Electrons are not permitted to pass through the separator between the negative and positive electrodes. However, the Li^+ can travel across the separator and migrate between the CCC/PE interface and the ACC/NE interface. According to Fig. 1, the boundary conditions (BCs) for electrodes and electrolyte are as follows:

$$-\sigma_s^{eff,-}\frac{\partial\phi_s^-(x,t)}{\partial x}\bigg|_{x=L^-} = -\sigma_s^{eff,+}\frac{\partial\phi_s^+(x,t)}{\partial x}\bigg|_{x=L^-+L^{sep}} = 0 \quad (8a)$$

$$-\sigma_s^{eff,+}\frac{\partial\phi_s^+(x,t)}{\partial x}\bigg|_{x=L} = i_{app} \quad (8b)$$

where i_{app} is the current density applied to the battery electrode. Eq. (8a) indicates that there is no charge flux at the interfaces of the NE/separator and the separator/PE, whereas Eq. (8b) refers that the BCs at the CCC is proportional to i_{app}.

The ϕ_s at the cell's left and right ends are set to:

$$\phi_s^-(x,t)|_{x=0} = 0 \quad (9a)$$

$$\phi_s^+(x,t)|_{x=L} = V_{cell} \quad (9b)$$

The cell potential (Voltage), V_{cell}, across the cell terminals is calculated as:

$$V_{cell}(t) = \phi_s^+(x,t)|_{x=L} - \phi_s^-(x,t)|_{x=0} - R_c\frac{I(t)}{A} \quad (10)$$

The quantity R_c is a contact resistance between the electrode and the current collector for a unit area surface. For a good battery, this is small and is sometime ignored in the analysis. A is the electrode area and I is the applied current in amps.

Because there is no ionic current in the current collector (CC), the electric intensity of the electrolyte phase at the cell's two ends is zero, is given by:

$$-\sigma_e^{eff,-}\frac{\partial\phi_e^-(x,t)}{\partial x}\bigg|_{x=0} = -\sigma_e^{eff,+}\frac{\partial\phi_e^+(x,t)}{\partial x}\bigg|_{x=L} = 0 \quad (11a)$$

The liquid phase current at the electrode/separator interface should be continuous, namely

$$-\sigma_e^{eff,-}\frac{\partial\phi_e^-(x,t)}{\partial x}\bigg|_{x=L^-(-)} = -\sigma_e^{eff,sep}\frac{\partial\phi_e^{sep}(x,t)}{\partial x}\bigg|_{x=L^-(+)} \quad (11b)$$

$$-\sigma_e^{eff,sep}\frac{\partial\phi_e^{sep}(x,t)}{\partial x}\bigg|_{x=(L^-+L^{sep})(-)} = -\sigma_e^{eff,+}\frac{\partial\phi_e^+(x,t)}{\partial x}\bigg|_{x=(L^-+L^{sep})(+)} \quad (11c)$$

Mass Conservation Equations

The mass conservation of Li^+ in the spherically-active material is represented by Fick's second law of diffusion which states that the molar flux due to diffusion is proportional to the concentration gradient.

$$\frac{\partial C_s^{\mp}(x,r,t)}{\partial t} = \frac{D_s^{\mp}}{r^2}\frac{\partial}{\partial r}\left(r^2\frac{\partial C_s^{\mp}(x,r,t)}{\partial r}\right) \quad (12)$$

where $C_s^{\mp}$ stand for the lithium concentration in the active material particles, $D_s^{\mp}$ represent the lithium diffusion coefficient in the active material. t and r denote the time and the radial coordinate within a spherical particle, respectively, while x is the particle location in x direction, see Fig. 1.

The mass conservation of Li^+ in the electrolyte can be described as:

$$\varepsilon_e^i\frac{\partial C_e^i(x,t)}{\partial t} + \frac{\partial J_l(x,t)}{\partial x} = \frac{a_s j_{loc}(x,t)}{F} \quad (13)$$

$C_e^i(x,t)$ and ε_e^i denote the Li-ion concentration in the electrolyte and the electrolyte volume fraction (porosity), respectively, while $J_l(x,t)$ is the Li-ions' molar flux and can be expressed as:

$$J_l(x,t) = -D_e^{eff,i}\frac{\partial C_e^i(x,t)}{\partial x} + \frac{i_e t_a^0}{F} \quad (14)$$

The first term of $J_l(x,t)$ follows Fick's law, whereas the second term accounts for electro-migration. t_a^0 is the transference number for the anion. $D_e^{eff,i}$ is the effective electrolyte diffusion coefficient, and can be calculated using Bruggeman's relation:

$$D_e^{eff,i} = D_e^i\varepsilon_e^{\beta,i} \quad (15)$$

where D_e^i represents the bulk diffusion coefficient in the liquid phase. ε_e^i and D_e^i are different values in each domain (anode, separator, and cathode). Substituting Eq. (14) into Eq. (13) we get:

$$\varepsilon_e^i\frac{\partial C_e^i(x,t)}{\partial t} = \frac{\partial}{\partial x}\left(D_e^{eff,i}\frac{\partial C_e^i(x,t)}{\partial x}\right) + \frac{1-t_a^0}{F}\, a_s j_{loc}(x,t) \quad (16)$$

The BCs of Eq. (12) are as follows:

The Li^+ concentration gradient equals zero at the sphere's centre ($r = 0$),

$$-D_s^{\mp}\frac{\partial C_s^{\mp}(x,r,t)}{\partial r}\bigg|_{r=0} = 0 \quad (17a)$$

The Li^+ diffusion rate equals the reaction rate at the sphere surface ($r = R_p^{\mp}$),

$$-D_s^{\mp}\frac{\partial C_s^{\mp}(x,r,t)}{\partial r}\bigg|_{r=R_p^{\mp}}=\frac{j_{loc}(x,t)}{F}=J_l(x,t) \qquad (17b)$$

At the spherical particle surface $C_s^{\mp}(x,R_p^{\mp},t)=C_{se}^{\mp}(x,t)$, describing the lithium concentration at the solid/electrolyte interface ($C_{se}^{\mp}$). The BCs for Eq. (16) are as follows:

The *Li*⁺ diffusion flux in the liquid phase equals zero at the electrode/current collector interface,

$$-D_e^{eff,-}\frac{\partial C_e^{-}(x,t)}{\partial x}\bigg|_{x=0}=-D_e^{eff,+}\frac{\partial C_e^{+}(x,t)}{\partial x}\bigg|_{x=L}=0 \qquad (18a)$$

Since the LiB has three spatial domains, we require four extra BCs at the electrode/separator interface. These BCs are determined by the continuity of the flux and concentration of the electrolyte at the electrode/separator interface. The *Li*⁺ diffusion flux is continuous at the electrode/separator interface,

$$D_e^{eff,-}\frac{\partial C_e^{-}(x,t)}{\partial x}\bigg|_{x=L^-(-)}=D_e^{eff,sep}\frac{\partial C_e^{sep}(x,t)}{\partial x}\bigg|_{x=L^-(+)} \qquad (18b)$$

$$D_e^{eff,sep}\frac{\partial C_e^{sep}(x,t)}{\partial x}\bigg|_{x=(L^-+L^{sep})(-)}=D_e^{eff,+}\frac{\partial C_e^{+}(x,t)}{\partial x}\bigg|_{x=(L^-+L^{sep})(+)} \qquad (18c)$$

At the electrode/separator interface, the *Li*⁺ concentrations are equal as well,

$$C_e^{-}(x,t)\big|_{x=L^-(-)}=C_e^{sep}(x,t)\big|_{x=L^-(+)} \qquad (18d)$$

$$C_e^{sep}(x,t)\big|_{x=(L^-+L^{sep})(-)}=C_e^{+}(x,t)\big|_{x=(L^-+L^{sep})(+)} \qquad (18e)$$

The initial concentration of lithium in the electrodes and electrolyte are:

$$C_s^{\mp}(x,r,t)\big|_{t=0}=C_{s,o}^{\mp} \qquad (19a)$$

$$C_e^{i}(x,t)\big|_{t=0}=C_{e,o}^{i} \qquad (19b)$$

Electrochemical Reaction Kinetics

The electrochemical reaction rate on the surface of the electrode particles is usually governed by the Butler-Volmer equation which is used to couple a charge-species governing equation and is given by:

$$j_{loc}(x,t)=j_o^{\mp}(x,t)\left[exp\left(\frac{\alpha_a F}{R_o T}\eta^{\mp}(x,t)\right)-exp\left(-\frac{\alpha_c F}{R_o T}\eta^{\mp}(x,t)\right)\right] \qquad (20)$$

where α_a and α_c represent the anodic and cathodic charge transfer coefficients of the electrode reaction, respectively. Note that the sum of α_a and α_c must equal 1, however in this study, both α_a and α_c are set to 0.5.

The exchange current density, $j_o^{\mp}(x,t)$, provides a measure of the electrochemical reaction rate at the reversible potential when the over-potential (η) equals zero. This reflects the electron transfer rates, and can be determined as:

$$j_o^{\mp}(x,t)=F(k_s^-)^{\alpha_c}(k_s^+)^{\alpha_a}C_e^{\mp}(x,t)^{\alpha_a}\left(C_{s,max}^{\mp}-C_{se}^{\mp}(x,t)\right)^{\alpha_a}C_{se}^{\mp}(x,t)^{\alpha_c} \qquad (21)$$

where k_s^- and k_s^+ are the reaction rate constant for both anode and cathode, respectively, while $C_{s,max}^{\mp}$ and $C_{se}^{\mp}(x,t)$ are respectively the maximum *Li*⁺ concentration and the *Li*⁺ concentration on the surface of electrode particles.

The over-potential (η) is the difference between solid and electrolyte phase potentials minus the thermodynamic equilibrium potential of the solid phase and the reduction in the solid/electrolyte interphase (SEI) film potential. The local surface overpotential, $\eta^{\mp}(x,t)$, is defined as [30]:

$$\eta^{\mp}(x,t)=\phi_s^{\mp}(x,t)-\phi_e^{\mp}(x,t)-U_{eq}^{\mp}-j_{loc}(x,t)R_f \qquad (22)$$

R_f is the SEI film resistance produced at the electrode surface. The electrode open-circuit potential or the thermodynamic equilibrium potential, $U_{eq}^{\mp}$, is a function of the local state-of-charge at the surface of the active particle ($SoC_{surf}^{\mp}$) and temperature (T) which can be estimated using a Taylor's series expansion.

$$\begin{aligned}U_{eq}^{\mp}&=U_{eq,ref}^{\mp}\left(SoC^{\mp},T_{ref}\right)+\frac{\partial U_{eq}^{\mp}}{\partial T}\left(T-T_{ref}\right)\\&=U_{eq,ref}^{\mp}\left(SoC^{\mp},T_{ref}\right)+\frac{\Delta S^{\mp}\left(SoC^{\mp}\right)}{nF}\left(T-T_{ref}\right)\end{aligned} \qquad (23)$$

$\Delta S^{\mp}$ is the change in entropy $\left(\Delta S^{\mp}=nF\left(\frac{\partial U_{eq}^{\mp}}{\partial T}\right)\right)$, and n denotes the number of electrons transferred. Where the surface $SoC^{\mp}$ for both negative and positive electrodes can be expressed by the ratio of the *Li*⁺ concentration in the active material as:

$$SoC^{\mp}=\frac{C_{se}^{\mp}(x,t)}{C_{s,max}^{\mp}} \qquad (24)$$

Local state of charge (*SoC*) of Li_xC_6 negative electrode is:

$$SoC^{-}=x=\frac{C_{se}^{-}(x,t)}{C_{s,max}^{-}} \qquad (25a)$$

Local state of charge (*SoC*) of NMC111 positive electrode is:

$$SoC^{+}=y=\frac{C_{se}^{+}(x,t)}{C_{s,max}^{+}} \qquad (25b)$$

Thermal Energy Conservation Equation

During the discharge and charge processes of a LiB, heat will be generated and the LiB surface temperature will rise. As the discharge current increases, the LiB's temperature rises faster. High battery temperatures can impair battery performance and may even cause irreparable damage to the battery. The energy balance in the LiB is composed of three heat-generating source terms, two of which are irreversible (Q_{irrev}) while the other is reversible (Q_{rev}), where Q_{rev} is primarily produced only at the electrodes, Q_{irrev}, on the other hand, is generated throughout the battery, including in the electrolyte, separator, and electrodes, see Figure 1. The total heat generation (Q_{tot}) is the sum of the reversible reaction heat generation (Q_{reac}) caused by the electrochemical reaction, which is mainly related to the entropy change of the active electrode material, the irreversible polarization heat generation (Q_{pol}), which is attributed to the potential difference of polarization, and the ohmic heat generation (Q_{ohm}) that comes from the resistance in the transfer of electrons and Li^+ inside a battery. Because current collectors have a high electrical conductivity, the heat generated by them is often neglected. Hence, the total heat generation rate of the battery is given by,

$$Q_{tot} = Q_{rev} + Q_{irrev} = Q_{reac} + Q_{pol} + Q_{ohm} \tag{26}$$

$$Q_{reac} = a_s j_{loc}(x,t) T \frac{\partial U_{eq}}{\partial T} = a_s j_{loc}(x,t) T \frac{\Delta S}{nF} \tag{27}$$

$$Q_{pol} = a_s j_{loc}(x,t) \eta^{\mp}(x,t) \tag{28}$$

$$Q_{ohm} = -\, i_s \cdot \nabla\phi_s^{\mp}(x,t) \; - \; i_e \cdot \nabla\phi_e^{\mp}(x,t) \tag{29}$$

The first term of Ohm's law (Q_{ohm}) represents the electrical heat generated within the solid phase of the material due to the flow of electric current, whereas the second term represents the ionic heat generated in the electrolyte phase due to the ionic motion. Eq. (29) can be rewritten as:

$$\begin{aligned} Q_{ohm} = \sigma_s^{eff,\mp}\left(\frac{\partial\phi_s^{\mp}(x,t)}{\partial x}\right)^2 \\ -\Bigg[-\sigma_e^{eff,i}\left(\frac{\partial\phi_e^{i}(x,t)}{\partial x}\right)^2 + \frac{2R_oT\sigma_e^{eff,i}}{F}(1-t_c^0)\Bigg(1 \\ + \frac{dln\, f_{\pm}}{dln\, C_e(x,t)}\Bigg)\frac{\partial ln\, C_e^i(x,t)}{\partial x}\,\frac{\partial\phi_e^{\mp}(x,t)}{\partial x}\Bigg] \end{aligned} \tag{30}$$

To determine the temperature distribution in the battery cell, the energy conservation equation of heat conduction for the cell is described by Fourier's law as follows:

$$\begin{aligned} \rho_b C_{p,b}\frac{\partial T}{\partial t} = \frac{1}{r}\frac{\partial}{\partial r}\left(k_r r\frac{\partial T}{\partial r}\right) + \frac{1}{r^2}\frac{\partial}{\partial\varphi}\left(k_\varphi\frac{\partial T}{\partial\varphi}\right) \\ + \frac{\partial}{\partial z}\left(k_z\frac{\partial T}{\partial z}\right) + Q_{tot} \end{aligned} \tag{31}$$

where ρ_b and $C_{p,b}$ are the density and the specific heat capacity of the battery cell, respectively. k_r, k_φ and k_z represent the thermal conductivities in the radial, circumferential, and axial directions, respectively. The term found on the left side of Eq. (31) indicates the energy accumulated within the LiB cell, whereas the terms on the right side correspond to the rates of 3D heat conduction and volumetric heat generation.

Inside a LiB, there are several layers wound in a spiral form to create a cylinder: including the anode, cathode, separator, and electrolyte. Every part is made from materials with different thermal conductivities, impacting the battery's heat management. The specific arrangement and stacking of these components help enhance the batter's total functionality and its anisotropic thermal characteristics, which means heat conduction changes depending on the direction.

Materials exhibit anisotropy when their properties change depending on the direction of measurement. Anisotropy in LiBs is important because of the diverse thermal conductivities present in the battery's structure. This trait impacts the way heat is controlled in various sections of the battery, impacting overall performance and safety. Studying the anisotropic thermal conductivity (k) in LiBs is crucial for improving energy storage technologies by preventing high temperatures from causing degradation and potential safety hazards through proper heat dissipation.

The k value is greater along the battery sheet compared to the perpendicular direction. As a result, the k value is determined separately for radial and normal directions before being included in the numerical model.

The k in the axial and radial directions is defined as follows [31]:

$$k_\varphi = k_z = \frac{\sum k_i L_i}{\sum L_i} = \frac{k_{cc}^- L_{cc}^- + k^- L^- + k^{sep}L^{sep} + k^+ L^+ + k_{cc}^+ L_{cc}^+}{L_{batt}} \tag{32}$$

$$k_r = \frac{\sum L_i}{\sum \frac{L_i}{k_i}} = \frac{L_{batt}}{\frac{L_{cc}^-}{k_{cc}^-} + \frac{L^-}{k^-} + \frac{L^{sep}}{k^{sep}} + \frac{L^+}{k^+} + \frac{L_{cc}^+}{k_{cc}^+}} \tag{33}$$

$$\sum L_i = L_{batt} = L_{cc}^- + L^- + L^{sep} + L^+ + L_{cc}^+ \tag{34}$$

where k_i denotes the thermal conductivity of each individual layer material (i^{th}). L_i represents the material thickness constituting the i^{th} layer of the battery in the radial direction. In the axial direction of a cell, the i^{th} layer material comprises a variety of components, including the i^{th} layer cathode electrode active material (+), the positive current collector ($\overset{+}{cc}$), the anode electrode material (−), the negative current collector ($\overline{cc}$), and the battery separator (sep). L_{batt} denotes the thickness of the entire battery.

Similarly, the density (ρ_i), heat capacity ($C_{p,i}$) and thickness (L_i) of each component are utilized to examine the average values of the density (ρ_b) and heat capacity ($C_{p,b}$) of the whole battery as:

$$\rho_b = \frac{\sum \rho_i L_i}{\sum L_i} \tag{35}$$

$$C_{p,b} = \frac{\sum C_{p_i} L_i}{\sum L_i} \tag{36}$$

According to the Newton's cooling and radiative heat transfer laws, the boundary condition for energy conservation is expressed as:

$$- k\nabla T = - h(T_{amb} - T) - \varepsilon K_s(T_{amb}^4 - T^4) \qquad (37)$$

where h is the convective heat transfer coefficient and its value is set as low as 5 W m^{-2} K^{-1} [32]. ε is the battery surface's emissivity, K_s is the Stephen-Boltzmann constant (K_s = 5.67 × 10^{-8} $W/(m^2 \cdot K^4)$), T and T_{amb} represent the battery surface and ambient temperatures, respectively. However, because of the relatively limited operational temperature range, the influence of radiation is minimal and can be ignored in this study.

A symmetry boundary condition (BC) is specified on the symmetry axis (z). On the outer BC ($R = R_0$, $z = 0$, and $z = H$), heat dissipation is mainly due to convection, which is governed by Newton's law of cooling. The BCs are shown as following:

$$-k_r \frac{\partial T}{\partial r}\bigg|_{r=0} = 0 \qquad (38)$$

$$-k_r \frac{\partial T}{\partial r}\bigg|_{r=R_0} = h(T_{amb} - T) \qquad (39)$$

$$-k_z \frac{\partial T}{\partial z}\bigg|_{z=0} = -k_z \frac{\partial T}{\partial z}\bigg|_{z=H} = h(T_{amb} - T) \qquad (40)$$

Air Flow

Due to the relatively low air flow velocities and characteristic lengths involved in the present study, the air flow is laminar in all cases examined. The governing equations for the airflow passing through the battery cell during simulation are given by [33]:

The continuity equation:

$$\nabla \boldsymbol{u} = 0 \qquad (41)$$

The momentum conservation equation:

$$\rho_a \frac{\partial \boldsymbol{u}}{\partial t} + \rho_a(\boldsymbol{u}.\nabla)\boldsymbol{u} = \nabla.[-p\boldsymbol{I} + \mu(\nabla\boldsymbol{u} + (\nabla\boldsymbol{u})^T)] \qquad (42)$$

where ρ_a is the air density and $\boldsymbol{u}$ is air velocity vector. The energy conservation equation of air is:

$$\rho_a C_{p_a}\left(\frac{\partial T_a}{\partial t}\right) + \rho_a C_{p_a}(\boldsymbol{u}.\nabla T_a) = \nabla.(k_a \nabla T_a) + Q_{tot} \qquad (43)$$

where T_a is the air temperature and k_a and C_{pa} are the thermal conductivity and specific heat capacity of air, respectively. The battery's initial temperature is identical to the air inlet temperature (25 °C), implying that air at ambient temperature is utilized in the BTMS. For the coolant at the inlet and outlet boundaries, velocity and pressure BCs are applied.

Temperature and concentration-dependent (dynamic) parameters

In the current study, a commercial 18650 cylindrical *NMC*-graphite Li-ion battery cell with a nominal capacity of 1.78 Ah has been investigated. The reason for selecting *NMC* Li-ion cell is that batteries with such chemistries are widely used in electric vehicles, mobile facilities, and other electronic equipment [24]. The negative electrode active material and electrolyte used in this study are Li_xC_6 *MCMB* and $LiPF_6$ dissolved in a mixture of 3:7 EC: EMC, respectively, while *NMC* 111 is employed as the positive electrode. Because electrochemical parameters are strongly dependent on temperature or concentration, the thermal-electrochemical coupled model is inherently nonlinear. These parameters are the reaction rate constant ($k_s^{\mp}$), the diffusion coefficient of Li-ions in the solid ($D_s^{\mp}$) and liquid (D_e^i) phases, the electrolyte ionic conductivity (σ_e^i), the open circuit potential ($U_{eq,ref}^{\mp}$) at the reference temperature, and the entropy changes ($\frac{\partial U_{eq}^{\mp}}{\partial T}$).

The temperature dependence of the $k_s^{\mp}$ was expressed using the Arrhenius equation [34-36]:

$$k_s^-(T) = k_{ref}^- \, exp\left[\frac{E_s^-}{R_o}\left(\frac{1}{T_{ref}} - \frac{1}{T}\right)\right] \qquad (44)$$

$$k_s^+(T) = k_{ref}^+ \, exp\left[\frac{E_s^+}{R_o}\left(\frac{1}{T_{ref}} - \frac{1}{T}\right)\right] \qquad (45)$$

where k_{ref}^- and k_{ref}^+ are the activation energy for the rate constant of the anode and cathode at the reference temperature (T_{ref} = 25 °C), respectively, while E_s^- and E_s^+ are the reaction activation energies for the anode and cathode, respectively. Furthermore, the local state of charge of the positive electrode (SoC^+) can be determined by Eq. (24).

The temperature-dependent diffusivity coefficient in both the negative and positive electrodes is given by [32]:

$$D_s^-(T) = 1.4523 \times 10^{-13} \, exp\left[\frac{\psi_s^-}{R_o}\left(\frac{1}{T_{ref}} - \frac{1}{T}\right)\right] \qquad (46)$$

$$D_s^+(T) = 0.5 \times 10^{-13} \, exp\left[\frac{\psi_s^+}{R_o}\left(\frac{1}{T_{ref}} - \frac{1}{T}\right)\right] \qquad (47)$$

The parameters ψ_s^- and ψ_s^+ are the activation energy for diffusion of lithium respectively in the negative and positive electrodes. The concentration and temperature dependent diffusion coefficient in the electrolyte (D_e^i) is represented as [4,36]:

$$D_e^i(C_e, T) = 10^{\left(-4.43-\left(\frac{54}{T-229-0.005C_e}\right)-0.0022C_e\right)-4} \qquad (48)$$

The concentration and temperature dependent ionic conductivity in the electrolyte, σ_e^i, which is characterized by the parameters of $LiPF_6$ in a EC: EMC (3:7) mixture at 25°C, is given by [3]:

$$\sigma_e^i(C_e,T) = C_e(-10.5 + 0.074T - 6.69\times10^{-5}T^2 + 0.668C_e - 0.0178C_eT + 2.8\times10^{-5}C_eT^2 + 0.494C_e^2 - 8.86\times10^{-4}C_e^2T)^2 \quad (49)$$

The Li^+ transference number (t^0) can be expressed as:

$$t^0 = 2.67\times10^{-4}exp\left(\frac{833}{T}\right)\left(\frac{C_e}{1000}\right)^2 + 3.09\times10^{-3}exp\left(\frac{653}{T}\right)\left(\frac{C_e}{1000}\right) + 517\times10^{-3}exp\left(-\frac{49.6}{T}\right) \quad (50)$$

The thermodynamic factor ($\mathcal{V}_e$) associated with electrolyte activity that is temperature and Li-ion concentration dependent, can be stated as follows:

$$\mathcal{V}_e = \left(1 + \frac{dln\, f_\pm}{dln\, C_e(x,t)}\right)(1 - t_c^0) = \frac{1-0.363}{1-0.399}\left(0.601 - 0.24\sqrt{10^{-3}C_e} + 0.982[1 - 0.0052(T-294)]\sqrt{10^{-9}C_e^3}\right) \quad (51)$$

As indicated in Eq. (23), the open circuit potential ($U_{eq,ref}^{\mp}$) and entropy change ($\frac{\partial U_{eq}^{\mp}}{\partial T}$) are both dependent on the state of charge (*SoC*) and are determined by experimental methods. Eqs. (52) and (53) represent the curves of the open circuit potential for both the positive electrode ($U_{eq,ref}^{+}$) and the negative electrode ($U_{eq,ref}^{-}$) versus local *SoC* on the surface of the active particles at the reference temperature of 298 K for both Li_xC_6 and $Li_yNi_{1/3}Mn_{1/3}Co_{1/3}O_2$ electrodes [17, 32, 36].

$$U_{eq,ref}^{-} = 0.1493 + 0.8493exp(-61.79x) + 0.3824exp(-665.8x) - exp(39.42x - 41.92) - 0.03131\,tan^{-1}(25.59x - 4.099) - 0.00943\,tan^{-1}(32.49x - 15.74) \quad for\ [0.001 \le x \le 0.7908] \quad (52)$$

$$U_{eq,ref}^{+} = -10.72y^4 + 23.88y^3 - 16.77y^2 + 2.595y + 4.563 \quad for\ [0.3597 \le y \le 0.9555] \quad (53)$$

The entropy changes of Li_xC_6 negative electrode ($\frac{\partial U_{eq}^{-}}{\partial T}$) and $Li_yNi_{1/3}Mn_{1/3}Co_{1/3}O_2$ positive electrode ($\frac{\partial U_{eq}^{+}}{\partial T}$) are [17, 32, 36]:

$$\frac{\partial U_{eq}^{-}}{\partial T} = -107.75x^4 + 77.265x^3 - 14.327x^2 - 1.0731x + 0.3706 \quad for\ [0 \le x \le 0.4] \quad (54a)$$

$$\frac{\partial U_{eq}^{-}}{\partial T} = -252.6x^6 + 882.69x^5 - 1181.7x^4 + 734.11x^3 - 189.78x^2 + 2.7368x + 4.377 \quad for\ [0.4 \le x \le 1.0] \quad (54b)$$

$$\frac{\partial U_{eq}^{+}}{\partial T} = 0.0968y^6 + 1.6689y^5 - 4.3898y^4 + 3.5863y^3 - 1.0882y^2 + 0.1705y - 0.1048 \quad (55)$$

where x and y in Eqs. (52-55) refer to the number of lithium moles that exist in the negative electrode's graphite structure (Li_xC_6) and the structure of the lithium-nickel-manganese-cobalt-oxide of the positive electrode

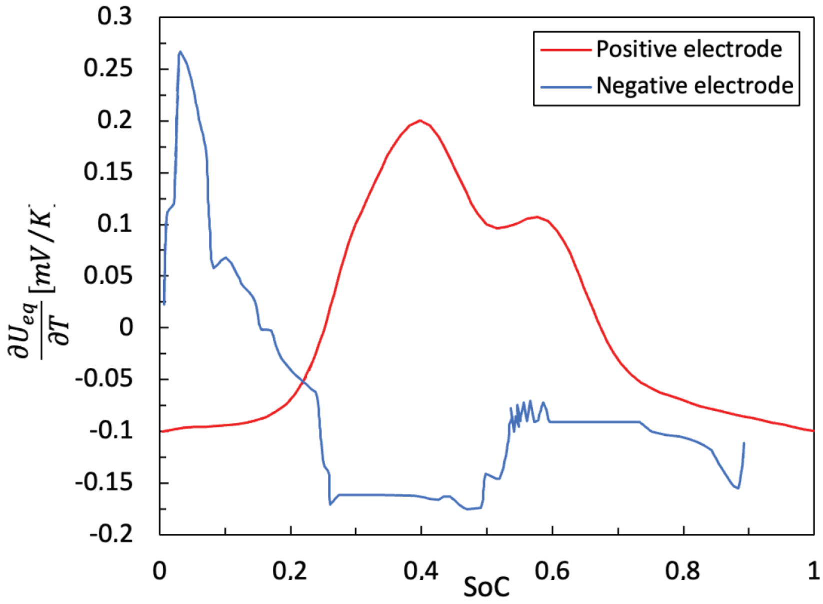

Figure 2. The entropy changes as a function of the SoC for both negative and positive electrodes.

($Li_yNi_{1/3}Mn_{1/3}Co_{1/3}O_2$), respectively. Figure 2 illustrates the entropy coefficient ($\frac{\partial U_{eq}^{\mp}}{\partial T}$) as a function of *SoC* for negative and positive electrodes and displays a difference between the two. This difference results from the open circuit voltage's hysteresis.

The cell nominal capacity (Q_c) in both electrodes of the NMC-graphite Li-ion battery cell can be estimated as [37]:

$$Q_c = \frac{AFL^- C_{s,max}^- \varepsilon_s^- (x_{100\%} - x_{0\%})}{3600} = \frac{AFL^+ C_{s,max}^+ \varepsilon_s^+ (y_{0\%} - y_{100\%})}{3600} [Ah] \quad (56)$$

$x_{0\%}$, $x_{100\%}$, $y_{0\%}$ and $y_{100\%}$ are the stoichiometry parameters of the anode and cathode at 0% and 100% cell SoC. The applied current density (i_{app}) for the electrochemical model at 1C-rate can be determined as [38, 39]:

$$i_{app,1C} = \frac{Q_c}{A} \quad (57)$$

where *A* is the electrode plate's area. Tables 1 and 2 list the battery's spatial and geometrical parameters, electrochemical kinetics, transport, and thermos-physical properties that were employed in the numerical simulation.

Table 1. Critical battery parameters used in the numerical model for a 1.78 Ah NMC 111 cylindrical 18650 type battery [3,32] [written permissions from the Elsevier]

Parameter	Units	Negative electrode	Separator	Positive electrode	Electrolyte	Cu foil	Al foil
Battery geometric parameters							
L_i	μm	40	25	36.297 [calculated]		10	15
R_p	μm	5		5			
ε_s	-	0.662		0.58			
ε_e	-	0.30	0.40	0.30			
$x_{0\%}$, $y_{0\%}$	-	0.001		0.955473			
$x_{100\%}$, $y_{100\%}$	-	0.790813		0.359749			
Lithium-ion concentrations							
$C_{s,max}$	mol/m^3	31,080		51,830			
$C_{s,o}$	mol/m^3	$0.215C_{s,max}$		$0.725C_{s,max}$			
$C_{e,o}$	mol/m^3				1,200		
Kinetic and transport parameters							
α_a, α_c	-	0.5		0.5			
β	-	1.5	1.5	1.5			
ψ_s	J/mol	42,770		18,550			
D_e	m^2/s				Eq. (48)		
D_s	m^2/s	Eq. (46)		Eq. (47)			
E_s	J/mol	37,480		39,575			
k_{ref}	$m^{2.5}/(mol^{0.5} \cdot s)$	1.764×10^{-11}		1.764×10^{-11}			
σ_e	S/m				Eq. (49)		
σ_s	S/m	10		0.1			
$\mathcal{V}_e$	-				Eq. (51)		
t_0	-		0.363				
Constant quantities							
T_{ref}	°C	25					
A	cm^2	1020.41					
Q_c	Ah	1.78 [calculated from Eq. (56)]					
$i_{app,1C}$	A/m^2	17.421 [calculated from Eq. (57)]					

Table 2. Thermophysical properties of materials used in the numerical model [3, 32]. [written permissions from the Elsevier]

Parameter	k $W/(m \cdot K)$	ρ kg/m^3	C_p $J/(kg \cdot K)$
$LiNi_{1/3}Mn_{1/3}Co_{1/3}O_2$ (NMC 111)	5.0	1500	700
Negative electrode (Graphite, Li_xC_6)	1.04	3600	1437.4
Separator	0.3344	1130	1978.16
Electrolyte $LiPF_6$	0.099	1210	1518
Cu foil	398	8933	385
Al foil	170	2770	875

NUMERICAL SIMULATION

Electrochemical and Thermal Coupling Strategy

In this study, a commercial software COMSOL Multiphysics 6.2, which is based on the finite element method (FEM), was employed to simulate the thermal behavior of a 3D axisymmetric of an air-cooled cylindrical 18650 Li-ion battery; see Figure 3(a and c). The strategy for coupling the electrochemical and thermal models is shown in Figure 3(b and c), in which the heat generated from the electrochemical part and the temperatures obtained from the thermal part are mutually used as inputs for each other. The electrochemical model can accurately simulate a battery's current-voltage response under pre-determined temperature conditions. By utilizing the simulated terminal voltage from the electrochemical model, the heat generation rate can be estimated and incorporated into the thermal model as a heat source term. The thermal model can then be solved numerically to obtain the temperature distribution within the LiB cell under the specified operating conditions. The battery's average temperature is subsequently determined and fed back into the electrochemical model to calculate the temperature-dependent electrochemical parameters. This iterative process enables a comprehensive understanding of the battery's thermal and electrochemical behaviour during operation.

In the thermal model, the heat transfer through the flow of air surrounding the LiB in a flow compartment is also

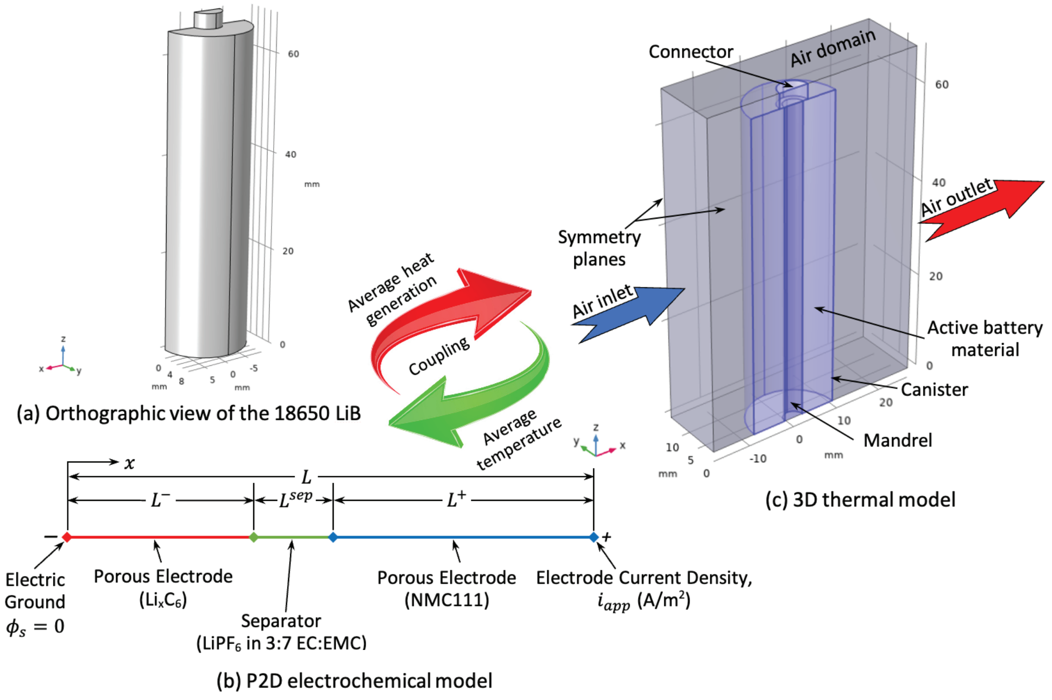

(a) Orthographic view of the 18650 LiB

(b) P2D electrochemical model

(c) 3D thermal model

Figure 3. Integrating P2D electrochemical model with 3D thermal model by utilizing average temperature and heat generation values.

accounted for using the Heat Transfer in Solids and Fluids interface in COMSOL, as depicted in Figure 3(c). This figure illustrates the incorporation of the flow of air into the thermal model, which is essential for accurately predicting the temperature distribution within the battery. By including the flow of air in the thermal model, the interface enables the simulation of the heat transfer mechanisms that occur between the battery and the surrounding air.

Once the solution has reached convergence at each time step, the data is post-processed to extract engineering-relevant quantities. Figure 4 depicts the algorithm flow chart for solving the governing equation. The segregated technique is used to couple the equations, which reduces memory usage and computing time. During each time step, two segregated steps are performed: initially, solving the temperature and flow with constant electrochemical variables; subsequently, using the temperature results to update local electrochemical parameters; and lastly, calculating the electrochemical variables for each mesh node. The procedure continues at every node until all variables have reached convergence. The direct solver PARDISO (Parallel Direct Sparse Solver Interface) was utilized as linear solver. Convergence happens at each time step when the relative tolerance for all variables is below 10^{-3}. The time increment persists until reaching the cut-off potential.

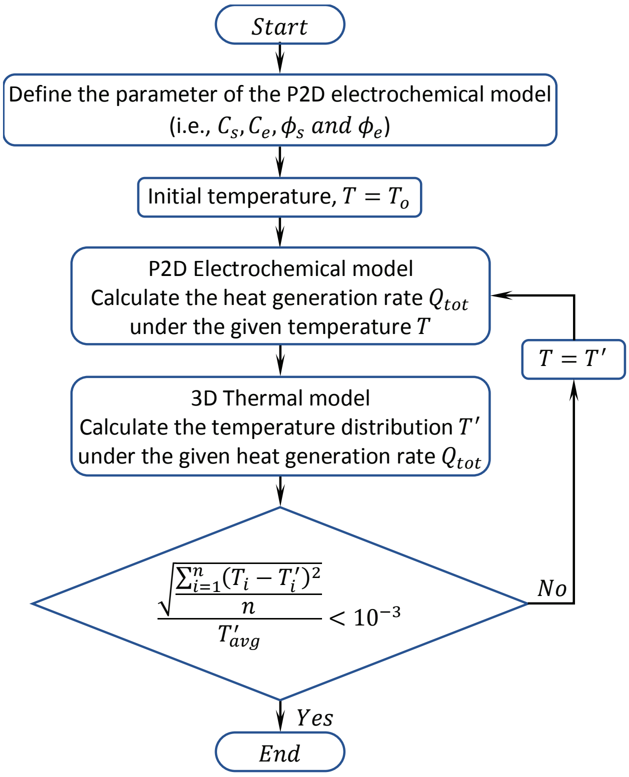

Figure 4. Solution algorithm employed to solve the governing equation (algorithm flow chart).

The thermal model's geometry is composed of several distinct domains, including the:

- Active battery material domain: this domain encompasses the wound sheets of battery cell material, which are 65 mm in height and have a radius of 9 mm.
- Mandrel domain: this domain represents the nylon isolator that surrounds the battery cell sheets, with a radius of 2 mm.
- Cylindrical battery connector domain: this domain consists of the steel connector that is placed on top of the battery, with a thickness of 3 mm.
- Flow compartment domain: this domain represents the air flow compartment within the battery.

Table 3 displays the dimension of all the above-mentioned components. The battery's initial temperature and the domain's inlet temperature are both specified at 25 °C, while an outflow condition is imposed at the domain's exit. However, all other external boundaries are thermally isolated. The flow has a specified velocity at the entrance and a constant pressure of 1 atm at the exit. No slip and symmetry BCs are applied to the battery walls and the symmetry planes, respectively.

In the electrochemical model, the negative electrode's current collector is maintained at 0V for the electronic current balance, while the positive electrode's current collector is set to a specific current density (i_{app}), as shown in Figure 3(b). The LiB numerical simulation is solved in three steps. The first step involves solving the steady-state flow at a temperature of 25 °C. In the second step, the potentials within the battery model are determined at an initial time of $t = 0$. The last step involves a time-dependent analysis of the entire problem, with the steady-state solution from the first two steps serving as the initial values for the potentials.

In the simulations, the initial ambient temperature was set at a fixed value of 25 °C and the battery cell is set to an initial SoC of 10%. A square wave function was utilized to alternate the charging and discharging current four times at a 2C rate with a cycle time of 500 s, then followed by a 500 s relaxation period after 2000 s, as shown in Figure 5. The relationship between cell voltage and C-rate is elucidated in Figure 5. It is observed that the cell voltage drops when the C-rate is negative, indicating that the battery is undergoing discharge. Conversely, as the C-rate approaches zero,

Table 3. Cell component size used in the numerical model

Parameter	Value	
r_{cell} $[mm]$	9	Cell radius
h_{cell} $[mm]$	65	Cell height
$r_{mandrel}$ $[mm]$	2	Mandrel radius
$r_{ceonnector}$ $[mm]$	3	Connector radius
$h_{ceonnector}$ $[mm]$	3	Connector height
t_{can} $[mm]$	0.25	External can thickness

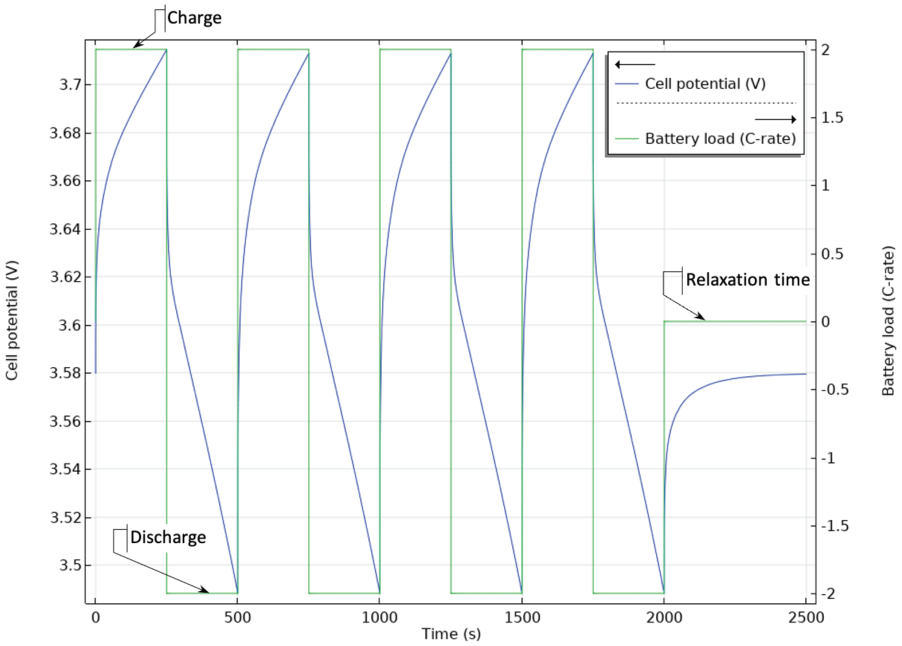

Figure 5. The simulated battery load and potential curve at 2C.

the cell voltage stabilizes, suggesting that the battery is not in use. Furthermore, an increase in the C-rate results in a corresponding rise in the cell voltage, indicating that the battery is being charged.

Mesh Sensitivity Analysis

To conduct a comprehensive sensitivity analysis of the electrochemical model, a series of four different mesh configurations were constructed at varying levels of refinement. These meshes, designated as coarse, fine, extra fine, and extremely fine, were created to assess the impact of mesh resolution on the model's predictions, see Figure 6(a). To enhance computational accuracy, refinement is applied to both sides of the separator for each of the four mesh types. In the thermal model, both hexahedral and tetrahedral

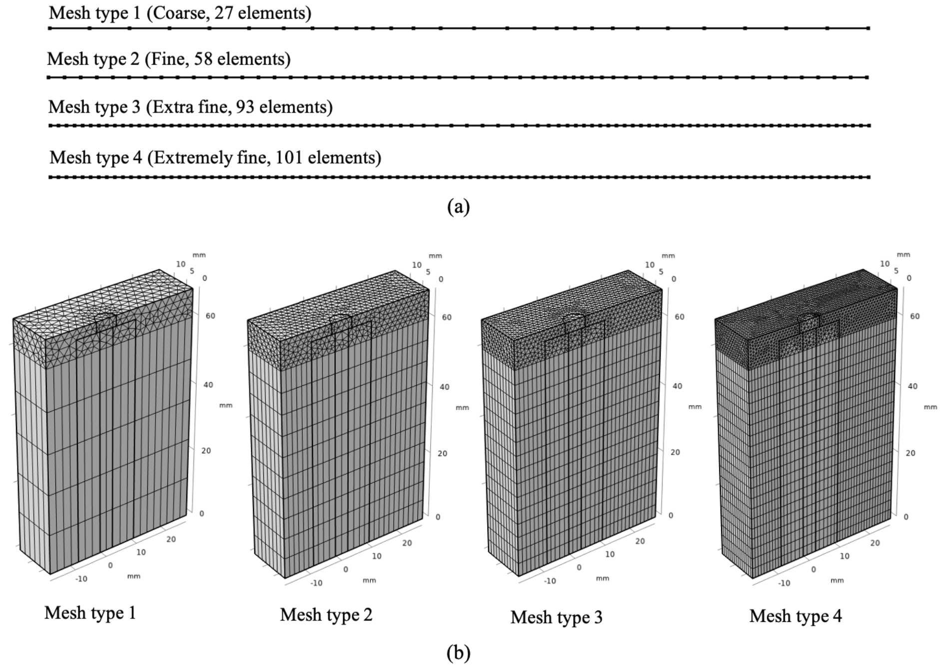

Figure 6. (a) P2D Electrochemical model at various meshes; (b) 3D thermal model at various meshes.

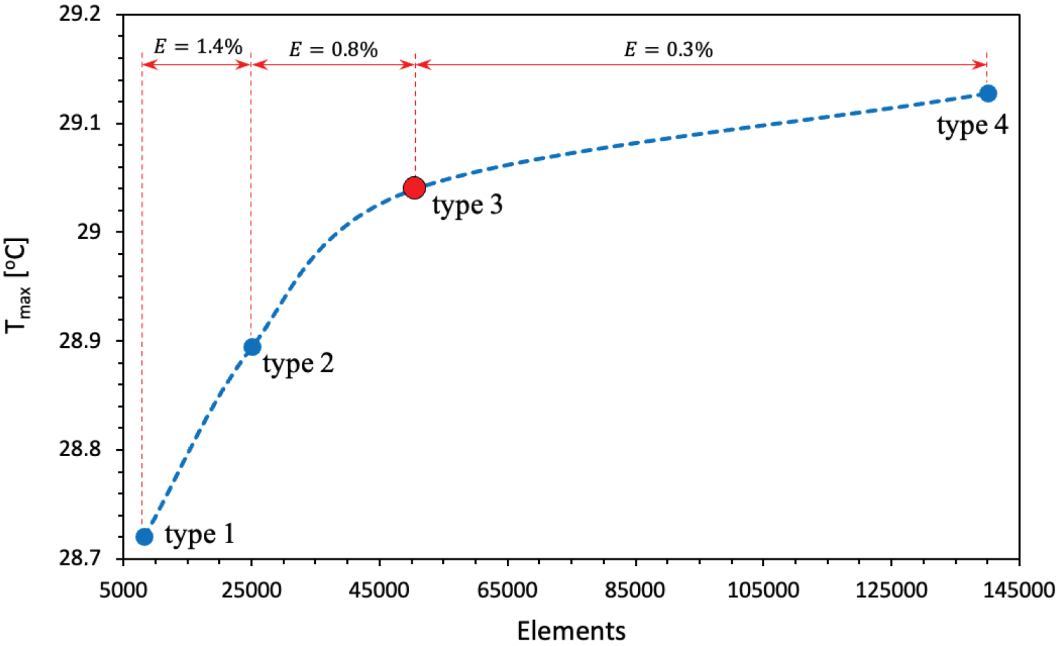

Figure 7. Maximum temperature of the LiB cell as a function of the number of elements.

elements were coupled for discretization, as illustrated in Figure 6(b). The mesh sensitivity analysis is carried out in the same manner with four types, each of which contains 8265 (type 1), 25103 (type 2), 50771 (type 3), and 140183 (type 4) elements and matches directly with the mesh types of the electrochemical model.

In this simulation, a PARDISO solver was selected with a relative tolerance of 10^{-3} for all variables, and solutions were evaluated for mesh independence. The computational time required to solve the problem on a computing platform with 8-core processors (operating at 2.60 GHz) and a total of 2 × 16 GB RAM was approximately two hours.

The maximum temperature (T_{max}) of the battery at the end of the discharge process (t = 2000 s) is displayed in Figure 7 with a C-rate of 2C. The ambient temperature (T_{amb}) was specified to be 25°C and the inlet airflow velocity (V_{in}) was 0.1 m/s. Figure 7 provides a comprehensive analysis of the impact of varying mesh sizes on the accuracy of numerical simulations. It should be noted that the relative error between types 3 and 4 mesh is roughly 0.3%. This finding indicates that any further increment in the number of elements will have a minimal effect. As a result, based on the trade-off between calculation cost and precision, type 3 mesh was adopted as the grid meshing strategy in the subsequent numerical simulations.

Model Validation

The experimental data from Kang et al. [17] is used to verify the accuracy of the numerical model. Experimental measurements and corresponding numerical simulations of the variation of the constant-current discharge process of the NMC/graphite 18,650-sized cylindrical battery cell with the elapsed time of discharge at three different discharge rates of 1, 2, and 3 C are shown in Figure 8. In this comparison, the ambient temperature was set at 25 °C, and the discharge cut-off voltage was maintained at 2.7 V. The boundary conditions applied for validation are: Eqs. 8 (a and b), Eqs. 9 (a and b), and Eqs. 11 (a, b and c) for charge conservation; Eqs. 17 (a and b), Eqs. 18 (a - e), and Eqs. 19 (a and b) for mass conservation; and Eqs. 38 – 40 for thermal energy.

Figure 8 shows how the discharge voltage and battery temperature changes during the discharge process. Figure 8(a) compares predicted and measured voltages across the battery over time; the figure shows that the experiments and simulations agree well for all discharge rates. It is observed that as the discharge rate increases (i.e., 3C), the voltage and elapsed time of discharge decrease in comparison to those at 1C. Figure 8(b) illustrates the variations of battery temperature with time during the discharge processes. It is evident that as the discharge rate increases, a concomitant increase in temperature is observed. The slight discrepancy between the experiment and the simulation may be attributed to the use of default values of the battery material parameters. The latter were sourced from the literature, and may vary with the temperature and therefore deviate from their default values. However, in general, the overall agreement between the experiments and numerical simulations is good.

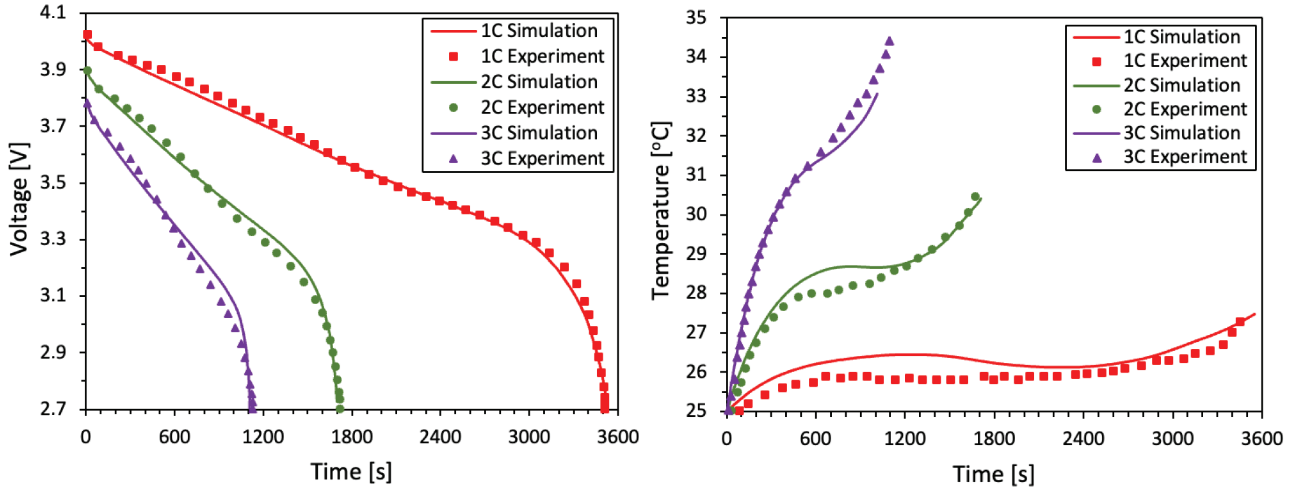

a) b)

Figure 8. (a) The discharge process of the experimental data and the battery model for discharge rates of 1C, 2C, and 3C. (b) The average temperature of the experimental data and the battery model while being discharged at rates of 1C, 2C, and 3C.

RESULTS AND DISCUSSION

Effects of Inlet Airflow Velocity on Battery Thermal Characteristics

The influence of inlet airflow velocity (V_{in}) was investigated numerically using four different velocities ranging from 0.1 to 0.7 m/s with a 0.2 m/s increment. Figure 9 illustrates the effect of the V_{in} on the maximum temperature (T_{max}) of the battery at 2C. As expected, increasing V_{in} has a significant effect on battery temperature, and the results demonstrate that increasing V_{in} from 0.1 to 0.7 m/s reduced T_{max} from 29.04 °C to 26.29 °C, respectively. Note that the temperature gradually increases during each charge-discharge process until it reaches a maximum value at the end of the process (t = 2000 s), then falls sharply when the charge-discharge process stops. The disparity in heating rates between charge and discharge processes can be ascribed to a variation in entropy change ($\frac{\partial U_{eq}^{\mp}}{\partial T}$) for the charge and discharge reactions and this founding was also demonstrated in Jiang et al.'s study [40].

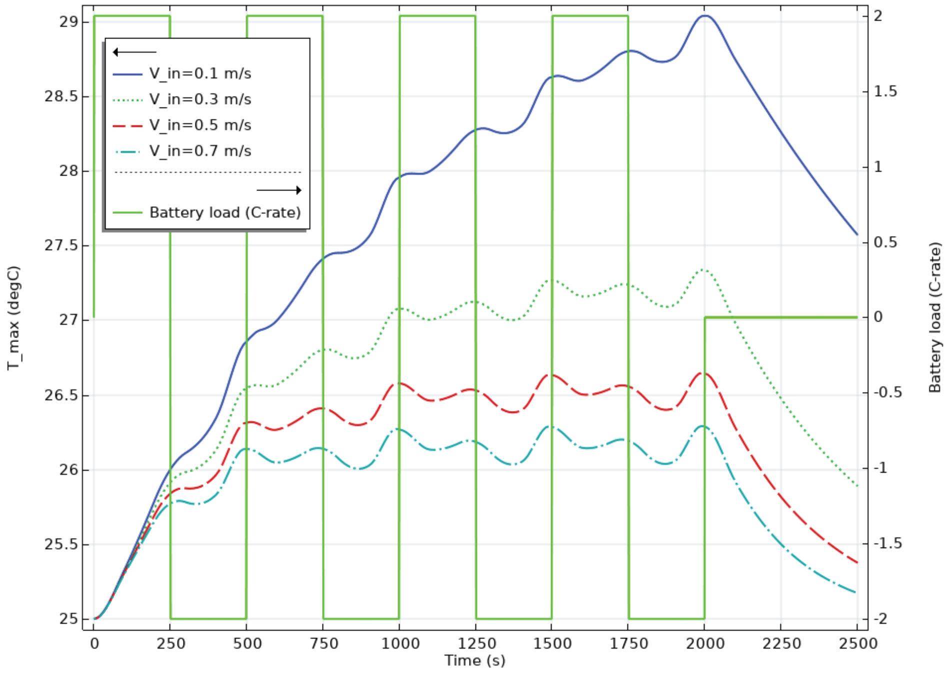

Figure 9. Effect of different inlet airflow velocities on the maximum temperature of the battery at 2C.

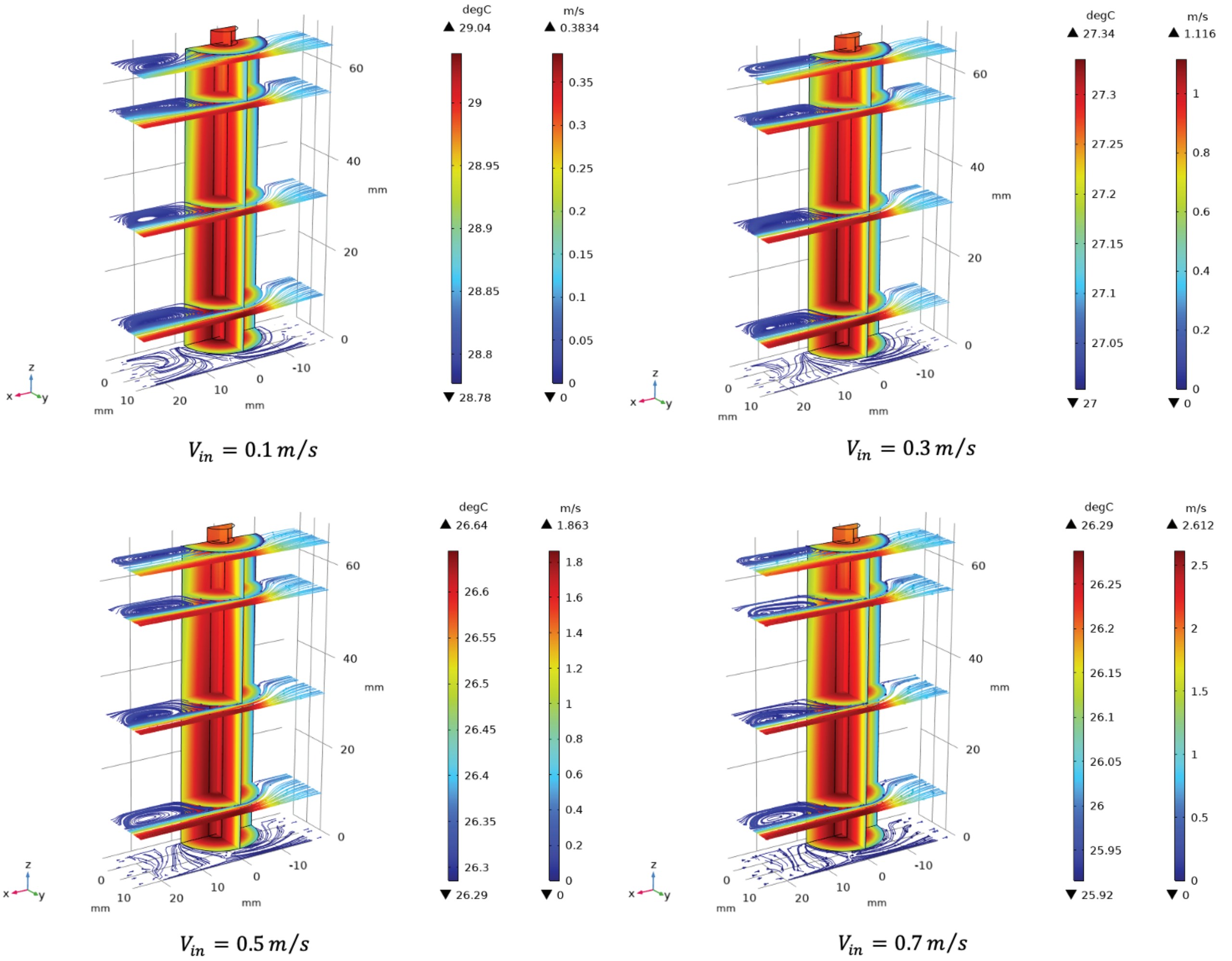

$V_{in} = 0.1\,m/s$ $V_{in} = 0.3\,m/s$

$V_{in} = 0.5\,m/s$ $V_{in} = 0.7\,m/s$

Figure 10. Internal temperature distribution of batteries within streamlines for the flow at 2000 s at different inlet airflow velocities.

Figure 10 presents the spatial distribution of the external flow field and internal temperature within a LiB cell during a charging-discharging process at a rate of 2C. Five multislices for both temperature and air streamlines are taken along the battery height at distances of 0, 10, 32.5, 55, and 65 mm from the base. The temperature distribution and airflow streamlines are presented at the completion of the charge-discharge processes (at time of 2000 s). The uneven distribution of internal temperature was evident, and this behavior was consistently observed at various inlet airflow velocities. The battery's lowest temperature was seen on the surface and near the air intake. The battery's interior temperature was highest at the mandrel and active battery material. Multiple factors, including internal resistance and electrochemical reactions, can lead to elevated temperatures at the mandrel and active battery material. Internal resistance can be influenced by both the mandrel and active materials. Increased resistance produces additional heat while operating. Particularly when experiencing high levels of current. During the process of charging and discharging, active battery materials experience electrochemical reactions. These reactions can generate heat, which might be more noticeable in specific areas, such as the mandrel, if it is positioned near high-energy zones. The battery's minimum and maximum temperatures decrease as V_{in} increased. Note also that the recirculating downstream air flows indicates that there will be pressure losses that will need to overcome through a hydraulic pumping power. The need to minimize these losses is another design consideration in electronic cooling systems.

Effects of Charge/Discharge Rate on LiB Thermal Characteristics

Increasing the C-rate for LiBs requires advancements across various aspects of battery design and materials. Improvements in electrode materials and design, electrolyte composition, battery architecture, thermal management, and battery management systems all contribute to enhancing the battery's ability to charge and discharge at higher rates. These factors collectively support the development of high-performance LiBs for applications that require rapid energy delivery and high-power density.

The battery's heat generation was simulated at four different charge/discharge rates of 1, 2, 4, and 6 C, and the variations in temperature within the LiB cell were numerically explored. At V_{in} = 0.1 *m/s* and an initial ambient temperature maintained at 25 °C, a battery with an initial SoC of 10% was utilized, which underwent four consecutive cycles of charging and discharging within a 500-second timeframe, totaling 2000 s. The maximum temperature of the battery at various charge/discharge rates is depicted in Figure 11. The simulation findings reveal that varied charge/discharge rates have a notable effect on LiB temperature. It is evident that the battery exhibited a relatively low temperature increase during charging and discharging processes at low rates of 1 C and 2 C, and the maximum temperature (T_{max}) was 26.2 °C and 29.0 °C, respectively. The battery's maximum temperature during high-rate discharge conditions (4C and 6C) resulted in temperatures reaching 40.0 °C and 57.9 °C, respectively, exceedingly twice that of the low-rate discharge. As a result, the effect of charge/discharge rate on LiB temperature exhibits a non-linear pattern, with increasing rates resulting in more significant temperature elevations, and this behavior was also shown in the Chiew et al.'s study [34]. This phenomenon occurs because the rise in internal resistance does not always follow a linear pattern in relation to the charging or discharging rate. Resistance can increase more notably at higher rates because of phenomena such as polarization effects, resulting in a more conspicuous temperature increase [35]. Note that these high temperatures may lead to permanent damage to the batteries and increase the risks associated with thermal runaway [6].

Charging and discharging a battery can significantly affect its temperature due to various electrochemical and physical processes occurring within the battery. Batteries have internal resistance, which converts part of the electrical energy into heat during charging. Higher currents can lead to more heat generation due to increased resistance. As the battery discharges, the current flowing through its internal resistance also generates heat. Higher discharge rates can lead to more heat due to increased resistive losses. As the charging rate increases, the faster the active material reacts, the faster the battery voltage increases, and the energy loss generated increases.

Figure 12 provides a visual representation of the spatial distribution of the exterior flow field and interior temperature of the LiB at V_{in} = 0.1 *m/s*. The interior temperature distribution is uneven, and this phenomenon is observed at various rates. The battery's lowest temperature is on the surface and in close proximity to the air inlet, while the battery's interior temperature was found to be significantly increased close to the battery center and the negative electrode. As the discharge rate increases, a corresponding rise in both the battery's minimum and maximum temperatures is observed.

High rates of charging and discharging entail extracting a large amount of current (requiring more Li^+) from the battery in a brief timeframe. This would result in a faster drop in voltage due to Ohmic polarization, caused by the increase in internal resistance. Layers of Li^+ will cover the electrode particles, hindering current flow and leading to a rise in internal resistance.

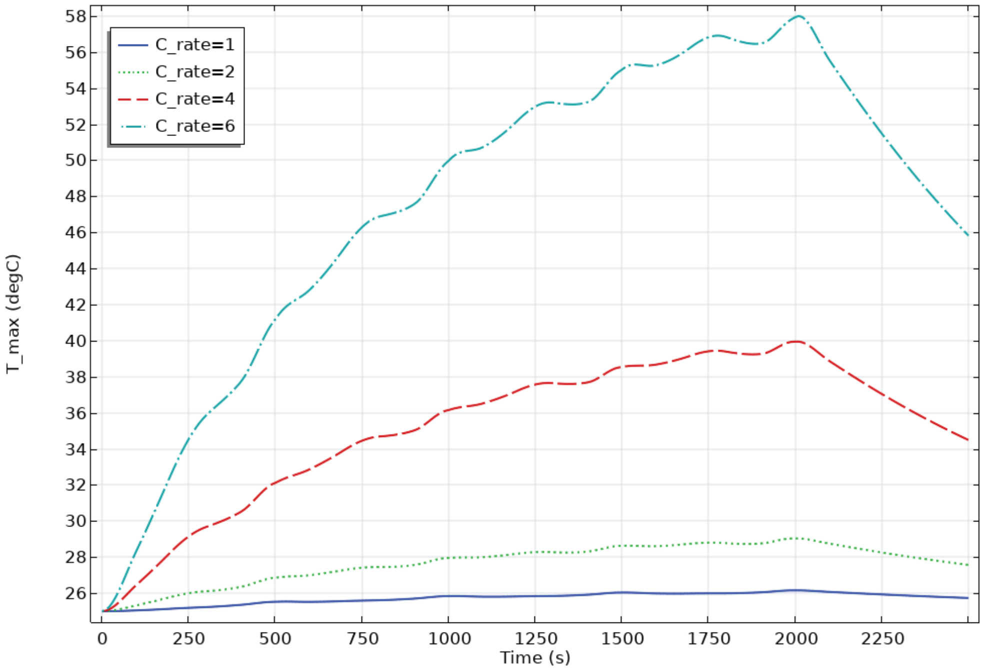

Figure 11. Effect of different charge–discharge rates on the maximum temperature of the battery at V_{in} = 0.1 *m/s*.

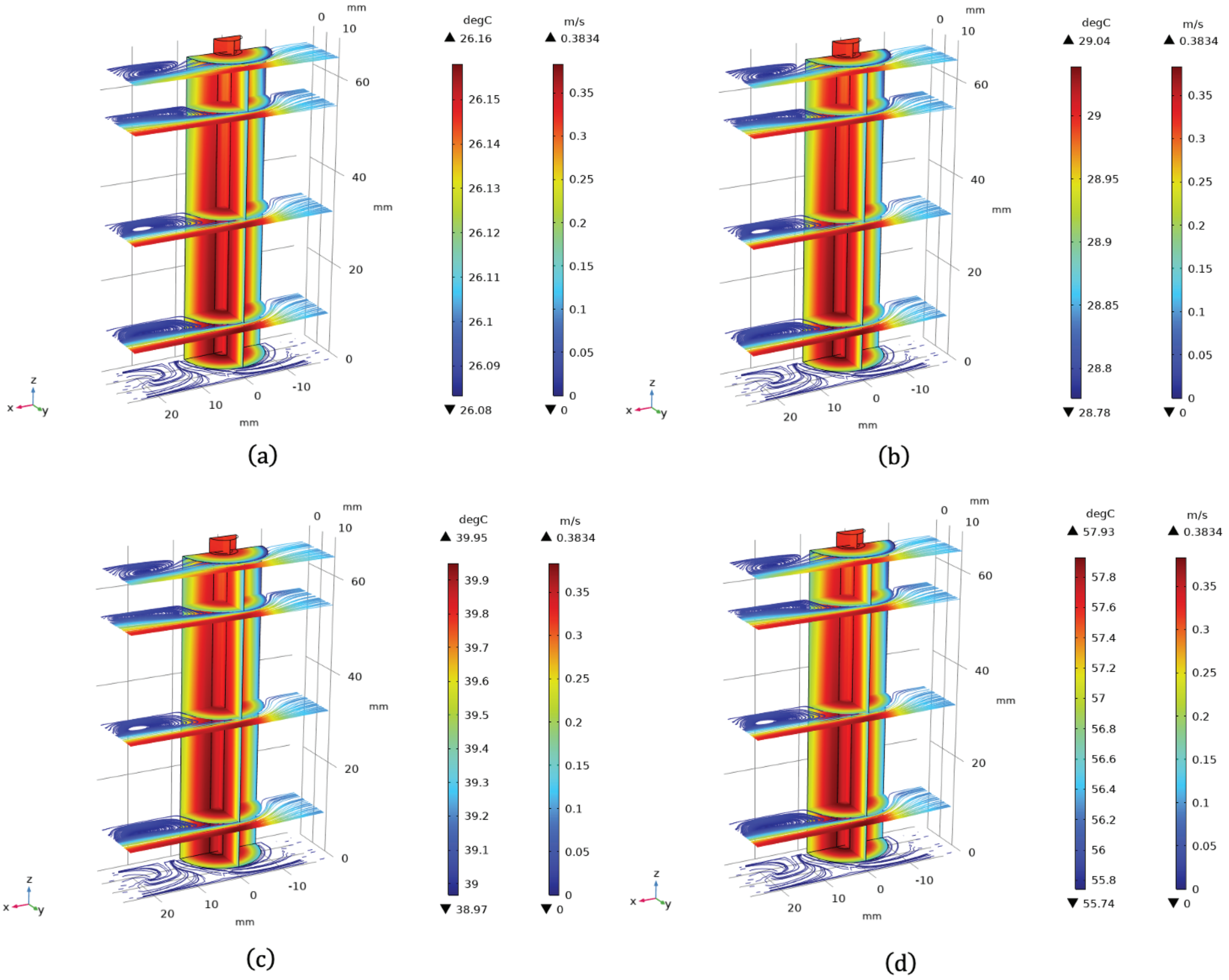

Figure 12. Battery interior temperature distribution at various C-rates. (a) 1C; (b) 2C; (c) 4C; and (d) 6C.

In the end, the battery reaches the cut-off voltage before being fully discharged, which impacts the discharge capacity.

Effects of Electrode Thickness on Battery Thermal Characteristics

The electrode thicknesses ($L^{\mp}$) effect on the thermal characteristics are now explored. In order to achieve a suitable balance between the capacity of the negative and positive electrodes in a LiB, the negative electrode thickness corresponds to the positive electrode thickness of (L^-, L^+) = (25 μm, 22.685 μm), (40 μm, 36.297 μm), (55 μm, 49.908 μm), and (70 μm, 63.519 μm) are employed. Eq. (56) can be used to estimate electrode capacity.

The battery capacity per unit area is estimated using the modelling parameters and Eq. (56), as indicated in Table 4. The ratio of negative electrode to positive electrode capacities per unit area of the LiB is known as N/P. When the battery's N/P ratio was maintained, L^- increased from 25 μm to 70 μm, and the capacity per unit area of the battery varied from 10.888 Ah/m^2 to 30.487 Ah/m^2. The positive electrode thickness decreased proportionally to the negative electrode thickness.

Table 4. The battery capacity at various anode and cathode thickness ratios

Anode thickness (μm)	Cathode thickness (μm)	Capacity (Ah/m^2)
25	**22.685**	10.888
40	36.297	17.421
55	49.908	23.954
70	63.519	30.487

Figure 13 displays the temperature variation of the LiB over time for four continuous charge-discharge processes at four different electrode thicknesses and discharge rates (1C, 2C, 4C, and 6C) when $V_{in} = 0.2\ m/s$. As can be seen, increasing L^- from 25 to 70 μm increased the maximum temperature (T_{max}) rise from 25.6 to 26.8 °C for a 1C discharge rate, 26.7 to 31.3 °C for a 2C discharge rate, 31.8 to 48.1 °C for a 4C discharge rate, and 40 to 74 °C for a 6C discharge rate. The observed relationship between the temperature increases of a LiB cell and the L^- can be attributed to the battery's nominal capacity, see Table 4. As the L^- increases, the electrode's surface area also increases, which enables more Li-ions to interact with the electrode and participate in the electrochemical reactions. This, in turn, enhances the battery's ability to store and release electrical energy, thereby increasing its nominal capacity, this finding also observed in the Kang et al.'s study [17].

The maximum temperature in (L^-, L^+) = (55 μm, 49.908 μm) and (70 μm, 63.519 μm) electrodes at 6C discharge rate exceeds the battery's optimal operating temperature range of 25 °C to 48 °C [41], potentially causing permanent damage to the battery and increase the risks associated with thermal runaway. Thus, a significant expansion in the electrode thickness will cause a dramatic increase in temperature, as well as a more non-uniform temperature distribution within the electrode, due to the reduced heat generation rate.

Thicker electrodes generally exhibit increased internal resistance and decreased ion diffusion, resulting in slower rates of charge and discharge. This may present an issue for applications that need quick charging, such as power tools or specific consumer electronics. Hence, optimizing electrode thickness entails balancing energy density with appropriate charge/discharge rates.

For thermal management, thicker electrodes can limit effective heat dissipation, resulting in higher operating temperatures and a higher scope of thermal runaway in thermal management. It is necessary to utilize effective thermal management techniques, such as advanced cooling systems or thermal interface materials. Keeping a consistent temperature throughout thicker electrodes is challenging, and

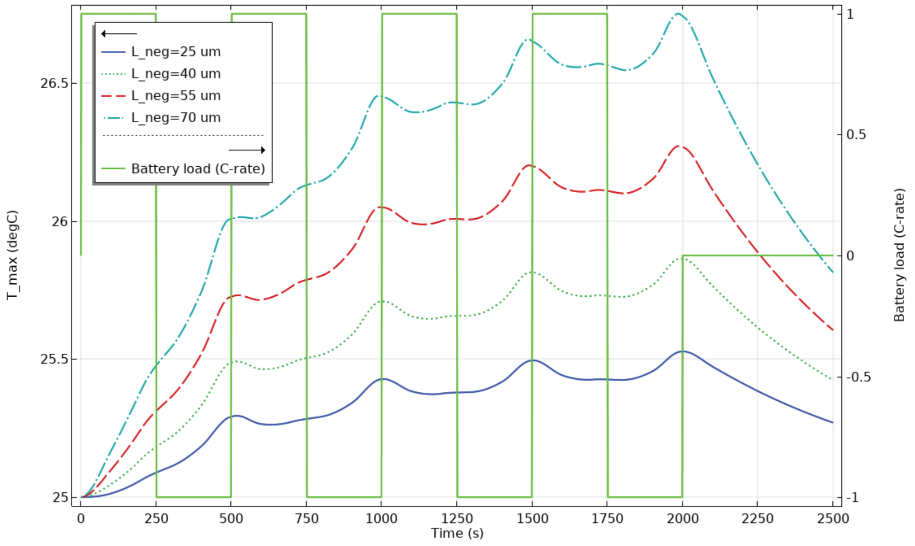

a)

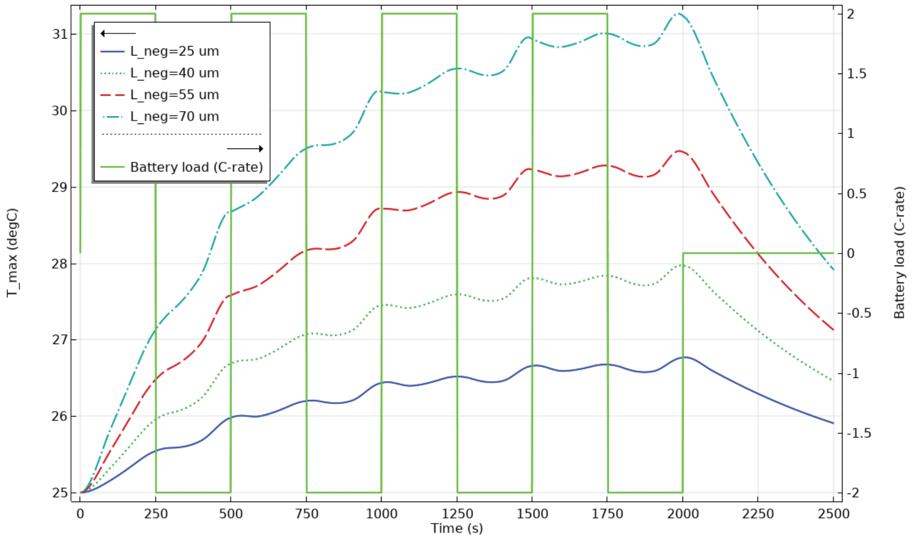

b)

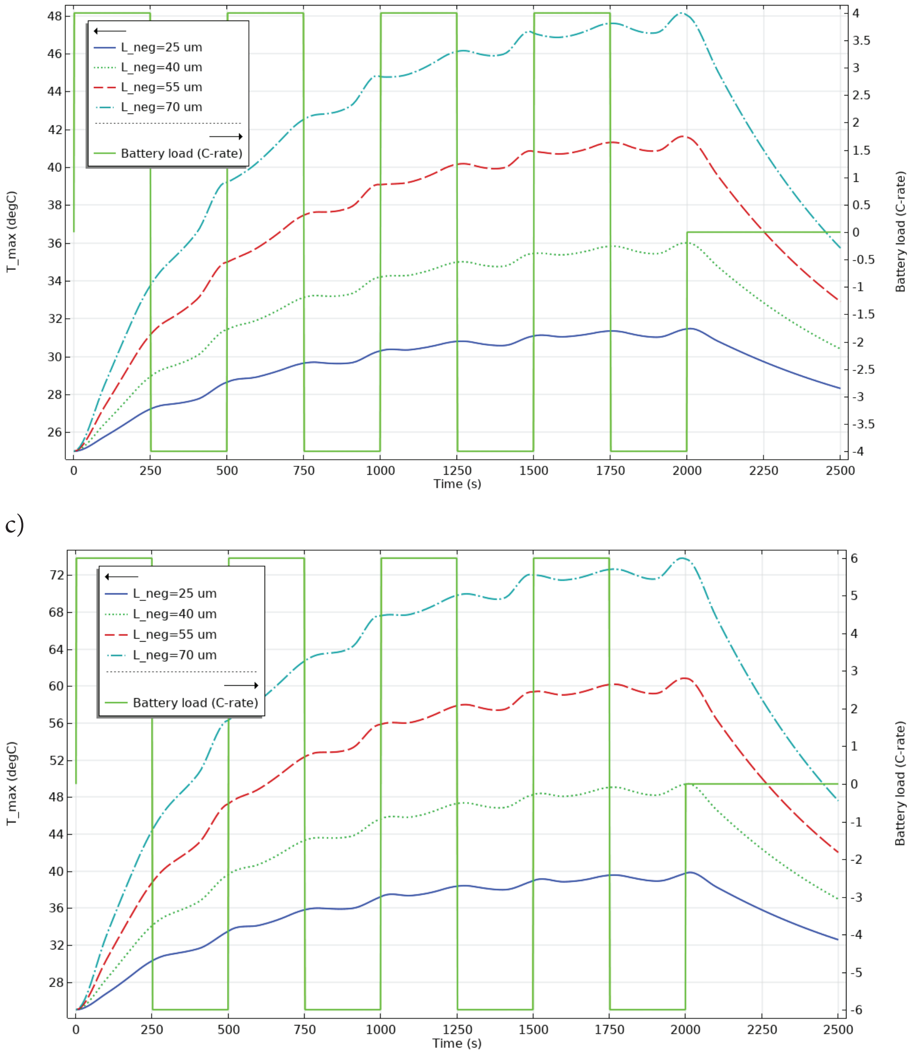

c)

d)

Figure 13. Effect of electrode thickness on the battery temperature with various charge/discharge rates. (a) 1C; (b) 2C; (c) 4C; and (d) 6C.

uneven temperatures can lead to localized deterioration and safety concerns. Changes in design may be necessary to ensure consistent temperature distribution.

In EVs, it is crucial to balance energy density and charge rate. Increased electrode thickness allows for greater driving distance; however, the charging infrastructure and battery management systems must be compatible with slower charging rates. For devices like laptops and smartphones, balancing battery life (energy density) and performance (charge/discharge rates) is essential. Increased electrode thickness could potentially extend battery longevity, however, it may also impact device performance and charging time.

Effect of Particle Size on Battery Thermal Characteristics

The particle size of electrode materials in LiBs is also very influential. To investigate this further, the positive active material particle size (R_p^+) was varied for four different values (1, 3, 5, and 7 μm) while maintaining the negative active material particle size (R_p^-) constant at 5 μm. Figure 14 shows the dependence of the maximum temperature (T_{max}) of the LiB cell with the different R_p^+ values at 4C charge–discharge rates and V_{in} = 0.2 m/s. It is clear that increasing R_p^+ enhances in the ability of Li^+ to intercalate and de-intercalate within the active particles, thereby leading to an increase in the heat generation rate and temperature. The results also show that increasing R_p^+ from 1 to 7 μm increased T_{max} significantly, from 32.06 °C to 38.74 °C (at time of 2000 s).

Figure 15 is a LiB cell temperature contour at 4C charge–discharge rates and V_{in} = 0.2 m/s. To observe the effect of R_p^+ on the temperature distribution, a cut plane was taken in the middle of the LiB cell (h_{cell} = 32.5 mm). The temperature distribution is presented at the completion of the

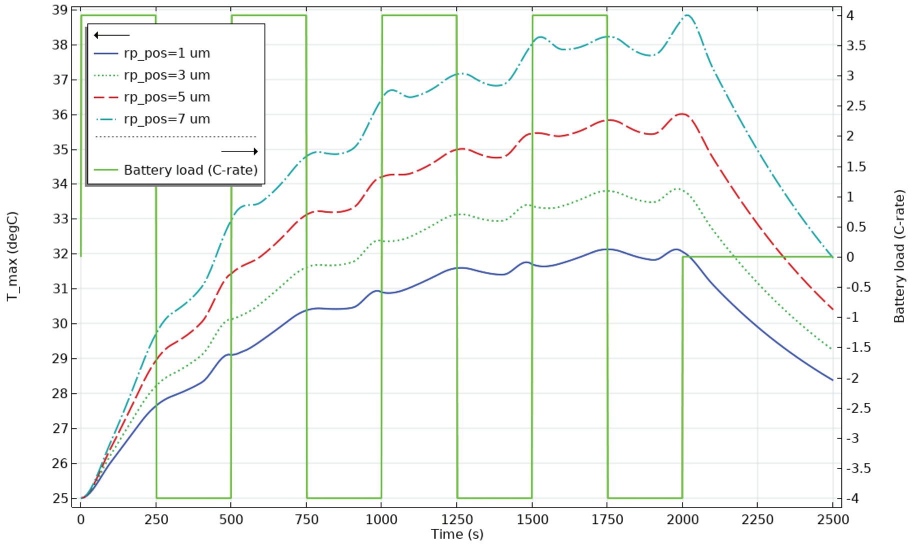

Figure 14. Effect of the cathode's particle size on the maximum temperature of the battery at 4 C charge–discharge rates and $V_{in} = 0.2\ m/s$.

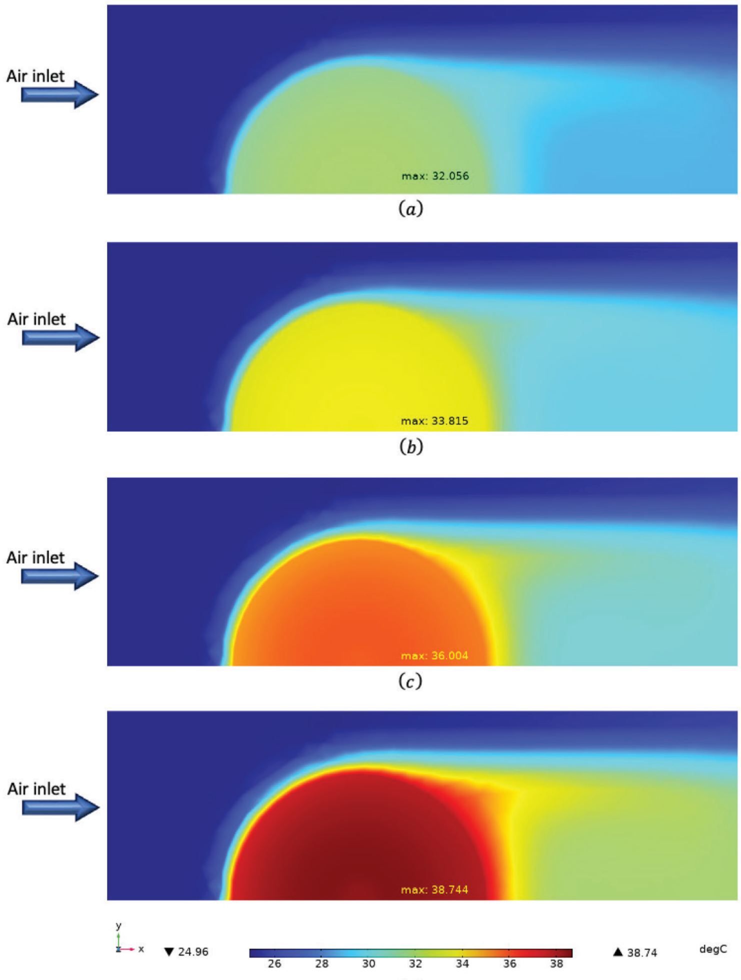

(*a*)

(*b*)

(*c*)

(*d*)

Figure 15. Temperature contour for the LiB cell at 4 C charge–discharge rates and ; at different (a) 1 μm; (b) 3 μm; (c) 5 μm; and (d) 7 μm.

charge-discharge processes (at time of 2000 s). As shown in Figure 15, the T_{max} was 38.74 °C at R_p^+ = 7 μm while the T_{max} was 32 °C at R_p^+ = 1 μm, a similar trend is noticeable in the study carried out by Liang et al. [42]. The reason for this is that larger particles have a smaller surface area-to-volume ratio than smaller particles. This decreased surface area may result in inefficient heat dissipation. In other words, there is a reduced surface area for heat generated in electrochemical reactions to dissipate from the active material, resulting in isolated temperature rises [18,19].

CONCLUSION

Keeping the temperature of LiBs under control is crucial for ensuring consistent performance and preventing safety issues related to thermal runaway, and maintaining reliability. In order to better predict and ultimately limit temperatures in LiBs, a novel mathematical model for the coupled electrochemical/thermal behavior of air-cooled, cylindrical LiBs is developed, enabling the impact of key parameters to be explored. Its application to the specific case of an 18,650-type NMC LiB module demonstrated that the inlet airflow velocity, charge-discharge rate (C-rate), electrode thickness and positive electrode particle size are all very influential and inappropriate choice of these parameters can result in high battery temperatures that could lead to battery damage and safety problems associated with thermal runaway.

Detailed numerical calculations for the 18,650-type NMC Li-ion battery module predict that

1. At a discharge rate of 2C, the results revealed that increasing the inlet airflow velocity from 0.1 to 0.7 m/s reduced the maximum temperature of the battery from 29.04 °C to 26.29 °C.
2. At an inlet airflow velocity of 0.1 m/s, under low charge/discharge rates (1C and 2C), the maximum temperature roughly increases by 2.8 °C (at t = 2000 s). However, at high charge/discharge rates (4C and 6C), there was a notable rise in maximum temperature, with an increase of 13.8 °C (at 4C) and 31.7 °C (at 6C) compared to the 1C case.
3. At an inlet airflow velocity of 0.2 m/s, the numerical calculations predict that increasing negative electrode thickness from 25 to 70 μm, maximum temperature increased from 40 °C to 74 °C at 6C compared with those at 1C from 25.6 °C to 26.8 °C. As a result, it is recommended that the LiB cell be operated with negative electrode thickness less than 55 μm at 6C.
4. At 4C charge–discharge rates and inlet airflow velocity of 0.2 m/s, the numerical results predict that raising positive electrode particle size from 1 to 7 μm increased maximum temperature from 32.06 °C to 38.74 °C (at time of 2000 s).

In the light of the above, conditions where the temperatures >40 °C will need to be managed carefully.

The performance of Li-ion BTMSs depend on a number of design parameters, including electrode thickness, electrode active material loading, electrode particle size and porosity, separator thickness, separator porosity, electrolyte concentration, and C-rate, and are subject to weight, space and costs constraints. In light of this future research should focus on the multi-objective optimization of the BTMS and carrying out detailed sensitivity analyses of the effect of its key design parameters. These studies will be both scientifically interesting and of great practical significance.

Finally, in light of the increasing popularity of liquid cooling in BTMSs the modelling approach developed here can be further applied to the design and optimization of the numerous liquid cooling technologies that have appeared recently.

NOMENCLATURE

A	Electrode area [m^2]
a_s	Specific surface area of the electrode [m^{-1}]
C_e	Lithium concentration in the electrolyte [mol/m^3]
C_p	Specific heat capacity [J/(kg.K)]
C_s	Lithium concentration in the active material particles [mol/m^3]
C_{se}	Lithium surface concentration in the active material [mol/m^3]
$C_{s,max}$	Maximum lithium concentration in the active material [mol/m^3]
D_e	Electrolyte diffusion coefficient [m^2/s]
D_s	Lithium diffusion coefficient in the active material [m^2/s]
E_s	Reaction activation energy [J/mole]
$f_\pm$	Average molar activity coefficient [−]
F	Faraday's constant [C/mol]
h	Convective heat transfer coefficient [W/(m^2.K)]
I	Applied current [A]
i_{app}	Battery applied current density [A/m^2]
i_e	Ionic current density in the electrolyte [A/m^2]
i_s	Solid-phase electrical current density [A/m^2]
J_l	Molar flux of lithium-ions [mol/(m^2.s)]
j_{loc}	Local charge transfers current density [A/m^2]
j_o	Exchange current density [A/m^2]
k	Thermal conductivity [W/(m.K)]
k_s	Reaction rate constant [m$^{2.5}$/(mol$^{0.5}$.s)]
K_s	Stephen-Boltzmann constant [W/(m^2.K^4)]
L	Electrode thickness [m]
L_{cc}	Current collector thickness [m]
n	Number of electrons transferred [-]
Q_c	Cell nominal capacity [Ah]
Q_{irrev}	Irreversible heat generation [W/m^3]
Q_{ohm}	Ohmic volumetric heat generation [W/m^3]
Q_{pol}	Polarization volumetric heat generation [W/m^3]
Q_{reac}	Reaction volumetric heat generation [W/m^3]
Q_{rev}	Reversible heat generation [W/m^3]
Q_{tot}	Total volumetric heat generation [W/m^3]
r	Radius distance variable of electrode particles [m]
R_o	Universal gas constant [J/(mol.K)]
R_p	Electrode particle radius [m]

S	Entropy [J/K]
t	Time [s]
t_a^0	Transference number for the anion [–]
t_c^0	Transference number for the cations [–]
T	Temperature [°C]
T_{amb}	Ambient temperature [°C]
T_{ref}	Reference temperature [°C]
U_{eq}	Electrode open-circuit potential [V]
$U_{eq,ref}$	Open-circuit potential at the reference temperature [V]
V_{cell}	Cell voltage [V]
ν_e	Thermodynamic factor of the electrolyte

Greek symbols

α_a	Anodic charge transfer coefficient [–]
α_c	Cathodic charge transfer coefficient [–]
ε	Emissivity of the battery surface [–]
ε_s	Active material volume fraction [–]
ε_e	Electrolyte volume fraction [–]
ρ	Density [kg/m^3]
σ_s	Electronic conductivity of the solid phase material [S/m]
σ_e	Ionic conductivity of the electrolyte [S/m]
ϕ_s	Solid phase potential [V]
ϕ_e	Electrolyte phase potential [V]
β	Bruggeman tortuosity exponent
η	Overpotential [V]
ψ_s	Diffusion activation energy [J/mol]
∇	Divergence

Subscripts and superscripts

+	Positive electrode (Cathode)
-	Negative electrode (Anode)
a	Air
amb	Ambient
b	Battery
cc	Current collector
e	liquid/electrolyte phase
eff	Effective value
max	Maximum
o	Initial value
ref	Reference value
s	Solid phase
sep	Separator
surf	Surface of active material particles

Acronyms

BTMS	Battery Thermal Management System
C	Discharge rate
DMC	Dimethyl Carbonate
EC	Ethylene Carbonate
EMC	Ethyl Methyl Carbonate
EVs	Electric Vehicles
HEVs	Hybrid Electric Vehicles
Li^+	Lithium ions
LiBs	Lithium-ion batteries
$LiCoO_2$	Lithium cobalt oxide
$LiFePO_4$	Lithium iron phosphate
$LiMnO_2$	Lithium manganese oxide
NCA	Nickel-Cobalt-Aluminum
NMC	Nickel-Manganese-Cobalt
P2D	Pseudo two-dimensional
SoC	State of Charge

ACKNOWLEDGEMENT

The authors would like to thank the University of Mosul for the facilities used in this study.

AUTHORSHIP CONTRIBUTIONS

Authors equally contributed to this work.

DATA AVAILABILITY STATEMENT

The authors confirm that the data that supports the findings of this study are available within the article. Raw data that support the finding of this study are available from the corresponding author, upon reasonable request.

CONFLICT OF INTEREST

The author declared they have no conflicts of interest regarding the research, authorship, and/or publication of this article.

STATEMENT ON THE USE OF ARTIFICIAL INTELLIGENCE

Artificial intelligence was not used in the preparation of the article.

REFERENCES

[1] Malima GC, Moyo F. Are electric vehicles economically viable in sub-Saharan Africa? The total cost of ownership of internal combustion engine and electric vehicles in Tanzania. Transport Policy 2023;141:14–26. [CrossRef]

[2] Yang Z, Yan Y, Pak U. Thermal reliability assessment and sensitivity analysis of 18,650 cylindrical lithium-ion battery. J Energy Storage 2023;59:106504. [CrossRef]

[3] Tanim TR, Rahn CD, Wang CY. State of charge estimation of a lithium ion cell based on a temperature dependent and electrolyte enhanced single particle model. Energy 2015;80:731–739. [CrossRef]

[4] He CX, Yue QL, Wu MC, Chen Q, Zhao TS. A 3D electrochemical-thermal coupled model for electrochemical and thermal analysis of pouch-type lithium-ion batteries. Intern J Heat Mass Transf 2021;181:121855. [CrossRef]

[5] Zhang Z, Yu W, Li H, Wan W, Zhang W, Zhuo W et al. Heat transfer characteristics and low-temperature performance of a lithium-ion battery with an inner cooling/heating structure. App Therm Eng 2023;219:119352. [CrossRef]

[6] Feng X, Zheng S, Ren D, He X, Wang L, Cui H et al. Investigating the thermal runaway mechanisms of lithium-ion batteries based on thermal analysis database. App Energy 2019;246:53–64. [CrossRef]

[7] Lu Y, Rong X, Hu YS, Chen L, Li H. Research and development of advanced battery materials in China. Energy Storag Mater 2019;23:144–153. [CrossRef]

[8] Liu Q, Qin L, Shi Q, Yao X, Xu C, Ju X. Optimization of the active battery immersion cooling based on a self-organized fluid flow design. J Energy Storag 2024;76:109851. [CrossRef]

[9] Satheesh VK, Krishna N, Kushwah PS, Garg I, Rai S, Hebbar GS et al. Enhancement in air-cooling of lithium-ion battery packs using tapered airflow duct. J Therm Eng 2024;10:375–385. [CrossRef]

[10] Chitta SD, Akkaldevi C, Jaidi J, Panchal S, Fowler M, Fraser R. Comparison of lumped and 1D electrochemical models for prismatic 20Ah $LiFePO_4$ battery sandwiched between minichannel cold-plates. App Therm Eng 2021;199:117586. [CrossRef]

[11] Gharde PR, Havaldar SN. Numerical investigation of an amalgamation of two phase change materials thermal energy storage system. J Therm Eng 2024;10:263–272. [CrossRef]

[12] Weng J, Huang Q, Li X, Zhang G, Ouyang D, Chen M et al. Safety issue on PCM-based battery thermal management: Material thermal stability and system hazard mitigation. Energy Storag Mater 2022;53:580–612. [CrossRef]

[13] Gungor S, Gocmen S, Cetkin E. A review on battery thermal management strategies in lithium-ion and post-lithium batteries for electric vehicles. J Therm Eng 2023;9:1078–1099. [CrossRef]

[14] Zhang T, Gao C, Gao Q, Wang G, Liu M, Guo Y et al. Status and development of electric vehicle integrated thermal management from BTM to HVAC. App Therm Eng 2015;88:398–409. [CrossRef]

[15] Luo J, Zou D, Wang Y, Wang S, Huang L. Battery thermal management systems (BTMs) based on phase change material (PCM): A comprehensive review. Chem Eng J 2022;430:132741. [CrossRef]

[16] Dong T, Peng P, Jiang F. Numerical modeling and analysis of the thermal behavior of NCM lithium-ion batteries subjected to very high C-rate discharge/charge operations. Intern J Heat Mass Transf 2018;117:261–272. [CrossRef]

[17] Kang J, Jia Y, Zhu G, Wang JV, Huang B, Fan Y. How electrode thicknesses influence performance of cylindrical lithium-ion batteries. J Energy Storag 2022;46:103827. [CrossRef]

[18] Xiao L, Guo Y, Qu D, Deng B, Liu H, Tang D. Influence of particle sizes and morphologies on the electrochemical performances of spinel $LiMn_2O_4$ cathode materials. J Power Sourc 2013;225:286–292. [CrossRef]

[19] Wang Y, Chen L, Wang Y, Xia Y. Cycling stability of spinel $LiMn_2O_4$ with different particle sizes in aqueous electrolyte. Elect Acta 2015;173:178–183. [CrossRef]

[20] Lu W, Jansen A, Dees D, Nelson P, Veselka NR, Henriksen G. High-energy electrode investigation for plug-in hybrid electric vehicles. J Power Sourc 2011;196:1537–1540. [CrossRef]

[21] Miranda D, Costa CM, Almeida AM, Mendez LS. Computer simulations of the influence of geometry in the performance of conventional and unconventional lithium-ion batteries. App Energy 2016;165:318–328. [CrossRef]

[22] Drake SJ, Martin M, Wetz DA, Ostanek JK, Miller SP, Heinzel JM, et al. Heat generation rate measurement in a Li-ion cell at large C-rates through temperature and heat flux measurements. J Power Sourc 2015;285:266–273. [CrossRef]

[23] Dasari H, Eisenbraun E. Predicting capacity fade in silicon anode-based li-ion batteries. Energies 2021;14:1448. [CrossRef]

[24] Miao Y, Hynan P, Jouanne AV, Yokochi A. Current li-ion battery technologies in electric vehicles and opportunities for advancements. Energies 2019;12:1074. [CrossRef]

[25] Cui X, Kam SK, Chin CM, Chen J, Babu C, Peng X. Models based on mechanical stress, initial stress, voltage, current, and applied stress for Li-ion batteries during different rates of discharge. Energy Storag 2020;2:1–10. [CrossRef]

[26] Warner J. The Handbook of Lithium-Ion Battery Pack Design Chemistry, Components, Types and Terminology. Amsterdam: Elsevier; 2015. p. 1–233. [CrossRef]

[27] Smith K, Wang CY. Solid-state diffusion limitations on pulse operation of a lithium ion cell for hybrid electric vehicles. J Power Sourc 2006;161:628–639. [CrossRef]

[28] Lam L, Bauer P, Kelder E. A Practical Circuit-based Model for Li-ion Battery Cells in Electric Vehicle Applications. IEEE 33rd International Telecommunications Energy Conference (INTELEC), 12 Decem 2011. Amsterdam, Netherlands: IEEE; 2011. s. 1-9

[29] Doyle M, Fuller TF, Newman J. Modeling of galvanostatic charge and discharge of the lithium/polymer/insertion cell. J Elect Soci 1993;14:1526–1533. [CrossRef]

[30] Tang Y, Wu L, Wei W, Wen D, Guo Q, Liang W, et al. Study of the thermal properties during the cyclic process of lithium ion power batteries using the electrochemical-thermal coupling model. App Therm Eng 2018;137:11–22. [CrossRef]

[31] Nie P, Zhang SW, Ran A, Yang C, Chen S, Li Z et al. Full-cycle electrochemical-thermal coupling analysis for commercial lithium-ion batteries. App Therm Eng 2021;184:116258. [CrossRef]

[32] Xie L, Huang Y, Lai H. Coupled prediction model of liquid-cooling based thermal management system for cylindrical lithium-ion module. App Therm Eng 2020;178:115599. [CrossRef]

[33] Kausthubharam, Koorata PK, Chandrasekaran N. Numerical investigation of cooling performance of a novel air-cooled thermal management system for cylindrical Li-ion battery module. App Therm Eng 2021;193:116961. [CrossRef]

[34] Chiew J, Chin CS, Toh WD, Gao Z, Jia J, Zhang CZ. A pseudo three-dimensional electrochemical-thermal model of a cylindrical $LiFePO_4$/graphite battery. App Therm Eng 2019;147:450–463. [CrossRef]

[35] Xu M, Wang X, Zhang L, Zhao P. Comparison of the effect of linear and two-step fast charging protocols on degradation of lithium ion batteries. Energ 2021;227:120417. [CrossRef]

[36] Wang QK, Shen JN, Ma ZF, He YJ. Decoupling parameter estimation strategy based electrochemical-thermal coupled modeling method for large format lithium-ion batteries with internal temperature experimental validation. Chem Eng J 2021;424:130308. [CrossRef]

[37] Li W, Cao D, Jöst D, Ringbeck F, Kuipers M, Frie F, et al. Parameter sensitivity analysis of electrochemical model-based battery management systems for lithium-ion batteries. App Energ 2020;269:115104. [CrossRef]

[38] Xu M, Wang R, Reichman B, Wang X. Modeling the effect of two-stage fast charging protocol on thermal behavior and charging energy efficiency of lithium-ion batteries. J Energ Storag 2018;20:298–309. [CrossRef]

[39] Bolsinger C, Birke KP. Effect of different cooling configurations on thermal gradients inside cylindrical battery cells. J Energ Storag 2019;21:222–230. [CrossRef]

[40] Jiang G, Zhuang L, Hu Q, Liu Z, Huang J. An investigation of heat transfer and capacity fade in a prismatic Li-ion battery based on an electrochemical-thermal coupling model. App Therm Eng 2020;171:115080. [CrossRef]

[41] Zhao D, Chen W. Analysis of polarization and thermal characteristics in lithium-ion battery with various electrode thicknesses. J Energ Storag 2023;71:108159. [CrossRef]

[42] Liang J, Gan Y, Yao M. Numerical analysis on the aging characteristics of a $LiFePO_4$ battery: Effect of active particle sizes in electrodes. J Energ Storag 2023;67:107546. [CrossRef]